Pulmonary Artery Hemodynamics Using MRI & CFD

By Jake Rabidou, M.S.B.E.

June 2017

Directed by: Stephanie George, Ph.D.

Department of Engineering

Pulmonary hypertension (PH), as defined by a mean pulmonary arterial pressure (mPAP) greater than 25 mmHg, is a life-threatening chronic disorder of the pulmonary circulation which leads to right ventricle failure and if untreated, death. The purpose of this work was to use both, magnetic resonance imaging (MRI) and computational fluid dynamics (CFD), to quantify changes in wall shear stress (WSS) throughout the pulmonary artery (PA) of a pulmonary hypertension (PH) population when compared to a normotensive control subject. With the future goal of this knowledge potentially being used to diagnose PH non-invasively. Patient's PA's were recreated using MRIs and MIMICS software. Velocity profiles were generated from the MRIs using MATLAB and CFD simulations were conducted using Fluent 17.0. Overall, the data followed a similar trend to published data where the control subject showed an approximately 1.5 to 3.5 times increase in WSS when compared to the PH subjects. The control subject showed a maximum of 5.596 dyn/cm^2 while the PH subjects ranged from 1.521 to 3.151 dyn/cm^2. This work can serve as the groundwork for further CFD simulations however, future work needs to be done with both a larger population size, potentially modeling further into the pulmonary vasculature as well as attempting different methods of data post-processing.

Pulmonary Artery Hemodynamics Using CFD & MRI

A THESIS

Presented to the Faculty of the Department of Engineering

College of Engineering and Technology

East Carolina University

In Partial Fulfillment of the Requirements for the Degree
Master of Science in Biomedical Engineering

By

Jake Rabidou

July 2017

Pulmonary Artery Hemodynamics Using MRI & CFD

By Jake Rabidou

Stephanie George, Ph.D., Director

Tarek Abdel-Salam, Ph.D., Reader

Jitka Virag, Ph.D., Reader

O. Hayden Griffin, Ph.D.
Chair of Engineering

Paul J. Gemperline, Ph.D.
Dean of the Graduate School

ACKNOWLEDGMENTS

This work was supported by East Carolina University's Department of Engineering. A special thanks to Dr. Bogdan Marcu for conducting the MRIs used in this study as well as confirming segmentation results, Dr. Maddipatti for referring patients to be subjects in this study, and, lastly, the study participants.

TABLE OF CONTENTS

Page

ACKNOWLEDGMENTS iv

LIST OF TABLES viii

LIST OF FIGURES ix

TERMS AND ABBREVIATIONS xi

CHAPTER

1. INTRODUCTION 1

1.1 Objective and Proposed Work 1

1.2 Organization of Thesis 2

2. BACKGROUND INFORMATION 3

2.1 Pulmonary Vasculature 3

2.2 Pulmonary Hypertension 4

2.2.1 Classification 4

2.2.2 Diagnosis 6

2.3 MRI in CFD 9

2.4 Introduction to CFD 10

2.4.1 Imaging 12

2.4.2 Phase Contrast MRI 14

2.4.3 Segmentation 14

2.4.4 Meshing 16

2.5 Introduction to Boundary Conditions 17

2.5.1 Inlet Boundary Conditions 17
2.5.2 Outlet Boundary Conditions 18

2.6 Solver Preferences 19
2.7 CFD Parameters 20
2.8 Current Pulmonary Artery CFD Models 21

3. METHODS 26

3.1 Experimental Methods 26

3.1.1 Subject Selection 26
3.1.2 Clinical Data 26
3.1.3 Image Acquisition 27
3.1.4 MRI Velocity Data Processing 29
3.1.5 MRI WSS Calculations 29

3.2 Numerical Methods 30

3.2.1 Geometry Creation 30
3.2.2 Geometry Post Processing 31
3.2.3 Meshing 31
3.2.4 Mesh Independence 32

3.3 Boundary Conditions and Fluid Properties 33
3.4 Running the Simulations 34

3.4.1 Solver Preferences 34

3.4.2 Convergence 34

3.5 Post Processing 36

3.6 Limitations 36

4. RESULTS 37

4.1 MRI Velocity Results 37

4.2 Validation Results 38

4.3 WSS Results 44

4.4 Velocity Results 50

4.4.1 CFD Velocity Results 50

5. DISCUSSION 61

6. CONCLUSION 68

REFERENCES 69

7. APPENDIX A: Supplemental Tables and Figures 75

APPENDIX B: IRB Approval 88

LIST OF TABLES

Table **Page**

2.1 Pulmonary Hypertension Categorization 5

3.1 Summary of Patient Information 27

4.1 MRI Calculated Data Summary (Averages) 37

4.2 CFD WSS Data Summary Pre-Increased Mesh Density 45

4.3 CFD WSS Data Summary Post-Increased Mesh Density 46

4.4 CFD Velocity Data Summary 51

7.1 Mesh Quality Data 76

7.2 Mesh Size Inputs 81

7.3 Mesh Independence Data 82

7.4 MRI Calculated Data Subject 14 83

7.5 MRI Calculated Data Subject 16 84

7.6 MRI Calculated Data Subject 17 85

7.7 MRI Calculated Data Subject 18 86

7.8 Mesh Quality Data Post-Increasing Density Near the Wall 87

LIST OF FIGURES

Figure **Page**

2.1 Pulmonary Vasculature 3

2.2 MRI Cross Section 14

2.3 Wall Shear Stress Distributions during Exercise (Tang 2011) 22

2.4 Wall Shear Stress Distributions (Tang 2012) 23

2.5 Wall Shear Stress Contour Map (Kheyfets 2015) 24

3.1 Sample Segmentation 30

3.2 Sample Mimics Model Pre-Smoothing 31

3.3 Sample Mesh Density Increased Near the Wall 32

3.4 Fluent Monitors vs. MRI Velocity Plots 35

4.1 Validation Comparison Subject 14 39

4.2 Validation Comparison Subject 16 40

4.3 Validation Comparison Subject 17 42

4.4 Validation Comparison Subject 18 43

4.5 WSS Plots Subject 14 47

4.6 WSS Plots Subject 16 48

4.7 WSS Plots Subject 17 49

4.8 WSS Plots Subject 18 50

4.9 Velocity Volume Renderings Subject 14 52

4.10 Velocity Volume Renderings Subject 16 53

4.11 Velocity Volume Renderings Subject 17 54

4.12 Velocity Volume Renderings Subject 18 55
4.13 Velocity Volume Renderings Subject 18 Post Increasing Mesh Density 56
4.14 Outlet Velocities over Time Subject 14 57
4.15 Outlet Velocities over Time Subject 16 58
4.16 Outlet Velocities over Time Subject 17 59
4.17 Outlet Velocities over Time Subject 18 60
7.1 Final Subject 14 Model and Mesh 77
7.2 Final Subject 16 Model and Mesh 78
7.3 Final Subject 17 Model and Mesh 79
7.4 Final Subject 18 Model and Mesh 80

TERMS AND ABBREVIATIONS

PH:	Pulmonary Hypertension
RHC:	Right Heart Catheterization
PAH:	Pulmonary Arterial Hypertension
PVH:	Pulmonary Venous Hypertension
WSS:	Wall Shear Stress
MPA:	Main Pulmonary Artery
LPA:	Left Pulmonary Artery
RPA:	Right Pulmonary Artery
PA:	Pulmonary Artery
CFD:	Computational Fluid Dynamics
MRI:	Magnetic Resonance Imaging
mPAP:	Mean Pulmonary Arterial Pressure
PCWP:	Pulmonary Capillary Wedge Pressure
TRV:	Tricuspid Regurgitation Velocity
PVR:	Pulmonary Vascular Resistance

CHAPTER 1

INTRODUCTION

1.1 Objective and Proposed Work

The overall objective of this thesis was to, through the use of magnetic resonance imaging (MRI) and computational fluid dynamics (CFD), quantify changes in wall shear stress throughout the pulmonary artery when compared to a normotensive control subject. With the future goal of this knowledge potentially being used to be able to diagnose pulmonary hypertension (PH) non-invasively using changes in wall shear stress (WSS). WSS is important because a reduction in WSS has been accepted as a known mechanism of endothelial dysfunction; and it has been suggested in literature that this reduction plays a role in PH pathogenesis; including the medial thickening, intimal fibrosis, and micro thrombosis, all of which can affect the pulmonary artery (Giad 1993, 1995; Botney 1999)

A comprehensive literature review on both pulmonary hypertension (PH) and CFD work in this field is included along with an introduction to the proposed methods that will be used in this study. Currently there is little research being done in this field in regards to using CFD to evaluate conditions in a strictly PH diagnosed population. With approximately 260,000 hospital each year due to pulmonary hypertension (Hyduk A. 2002). An estimated false diagnosis rate of 36% based on ECHO (Badesch 2009) and a compliance rate estimated at 60% (Sharma 2013) the need for a more accurate, less

invasive way to diagnose PH is greater than ever. This study as the potential to not only lead to a method of diagnosis, but also build off of other studies conducted in this field.

1.2 Organization of Thesis

Chapter 2 provides the background information on topics that support this work. These topics include (2.1) pulmonary vasculature, (2.2) pulmonary hypertension, including classification and diagnosis and (2.3) current literature. An introduction to CFD, boundary conditions, and various CFD parameters can be found in sections (2.4-2.7). Chapter 3 goes over both the experimental and numerical methods (3.1) and (3.2). Chapter 4 discusses the results of the study with MRI velocity results being discussed in (4.1). Validation results are discussed in (4.2) and wall shear stress results presented in (4.3). The CFD velocity results are presented in (4.4). Chapter 5 contains the discussion of the results and in Chapter 6, conclusions are drawn about the results.

CHAPTER 2

BACKGROUND INFORMATION

2.1 Pulmonary Vasculature

The pulmonary circulation is a highly specialized vascular bed that physically and functionally connects the heart and the lungs. The pulmonary circulation is the circulation of blood to and from the lungs. Unoxygenated blood from the right ventricle flows through the right and left pulmonary arteries to both the right and left lungs. After entering the lungs, the branches subdivide into smaller capillaries which surround the alveoli of the lungs and release carbon dioxide in exchange for oxygen. The capillaries unite and become veins; these veins join to form the pulmonary veins which return the oxygenated blood to the left atrium, to be pumped by the heart through the body. Figure 2.1, below shows a basic visualization of the pulmonary vasculature.

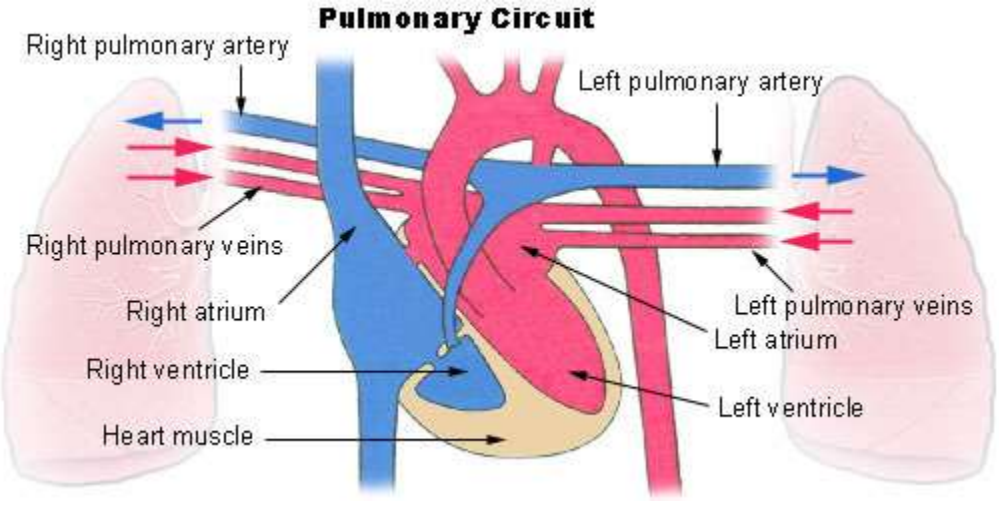

Figure 2.1 Visualization of the Basic Pulmonary Vasculature Oxygen Rich Blood is shown in Red while Oxygen Poor Blood is shown in Blue (Boundless 2016)

Throughout this thesis, the pulmonary artery will be the primary component of the pulmonary vasculature that is discussed and investigated. The pulmonary artery is the large artery originating from the superior surface of the right ventricle of the heart and carrying deoxygenated blood to the lungs for oxygenation; it starts as the pulmonary trunk which divides to form the right pulmonary artery that enters the right lung and the left pulmonary artery that enters the left lung.

2.2 Pulmonary Hypertension

Pulmonary hypertension (PH), as defined by a mean pulmonary arterial pressure (mPAP) greater than 25 mmHg, is a life-threatening chronic disorder of the pulmonary circulation which leads to right ventricle failure and if untreated, death (Botney 1999). With an overall prevalence of roughly 15 diagnosis per one million people per year (Humbert 2006); and varied prevalence ranging from 5-30% of high risk groups such as those with HIV, sclerosis, and sickle cell disease, this is a serious disease effecting thousands of people a year (Humbert 2006).

2.2.1 Classification

PH is classified according to underlying mechanism, clinical context, presentation, histopathology and response to treatment based on the most recent classification from the 5th World Symposium on PH in 2013 (Simonneau et al. 2013). Table 2.1 illustrates the five classifications.

Table 2.1 Categorization of PH (Simonneau 2013)

Group 1	Group 2	Group 3	Group 4	Group 5
Pulmonary arterial hypertension (PAH)	Pulmonary hypertension due to left heart disease	Pulmonary hypertension due to lung diseases and/or hypoxia	Chronic thromboembolic pulmonary hypertension (CTEPH)	Pulmonary hypertension with unclear multifactorial mechanisms

Group 1 represents pulmonary arterial hypertension (PAH), which is high pulmonary pressure due to elevated precapillary pulmonary resistance (Simonneau 2013). PAH is additionally characterized by a pulmonary capillary wedge pressure (PCWP) ≤ 15 (Shah 2012, Simonneau 2009). Patients, disregarding various other risk factors, with PAH have a mean life expectancy of 2.8 years in the absence of effective treatment (Mclaughlin 2006). A PCWP > 15 mmHg identifies Group 2, pulmonary venous hypertension (PVH). Pulmonary venous hypertension (PVH) refers to PH caused by left heart disease; this is typically a consequence of left atrial hypertension (Kulik 2014). The remaining three groups are separated by various other diseases that contribute to the progression of PH or in the case of Group 5, due to unclear multifactorial mechanisms. A known risk factor for PH is sickle-cell disease (SCD) (Group 1 PH); therefore, many diagnosed with PH may have SSD. A possible reason SCD is a risk factor for developing PH is that increased breakdown of red blood cells within the blood vessels cause inflammation and a decrease of nitric oxide (Pulmonary Hypertension

Association, 2013). This causes constriction of the pulmonary arteries which may lead to PH.

2.2.2 Diagnosis

Diagnosis of PH begins with non-invasive screening. Exercise intolerance, dyspnea, and exertional dizziness are all indicators in PH diagnosis (Shah 2012). Upon recommendation for further screening from a healthcare professional, traditionally PH is screened by using Doppler echocardiography (ECHO). In 2D ECHO, the echocardiogram produces an image of the heart, and the Doppler technology uses the Doppler affect to determine the direction and speed of blood flow (Badesch 2009). PH is diagnosed by 2D ECHO measuring a TRV ≥2.5 m/s or calculating a pulmonary artery systolic pressure (sPAP) ≥30 mmHg. A modified Bernoulli equation is then used to calculate the sPAP. When applying this equation, the two locations being analyzed are the right ventricle and the right atrium. In the right atrium, there is the right atrial pressure, and the TRV is representative of the velocity; while in the right ventricle you have pressure, but no velocity. There is also no change in height, because of this, all terms aside from the right ventricular pressure are known. Lastly, it is assumed that the right ventricle pressure is equal to the pressure in the pulmonary artery. The modified Bernoulli equation used is shown Equation 1 where Δp is equal to the change in pressure, between the right atrium and right ventricle and TRV is equal to the velocity of the tricuspid regurgitation:

$$\Delta p = 4 * TRV^2 \quad (1)$$

Patients with elevated TRV (≥2.5 m/s) are further evaluated using right heart catheterization (RHC) to confirm a diagnosis of PH and to differentiate between Group 1 and Group 2 (Hebson 2015). This procedure involves a physician guiding a special catheter called a pulmonary artery catheter to the right side of the heart. The physician then passes the tube into your pulmonary artery where they will observe blood flow through the heart and measures the pressures inside the heart and lungs. As the catheter advances toward the pulmonary artery, the physician will also measure pressures along the way, inside the chambers on the right side of the heart.

RHC is used for the diagnosis of PH and gives integral hemodynamic information used to distinguish between Group 1 and Group 2 PH. RHC measures systolic pulmonary arterial pressure (sPAP), diastolic pulmonary arterial pressure (dPAP), mean pulmonary arterial pressure (mPAP), pulmonary capillary wedge pressure (PCWP), and pulmonary vascular resistance (PVR) which are used to classify the patient into PH Groups, or normotensive. To measure these pressures, a balloon attached to the catheter is inflated at the varying locations and pressure changes are measured with a pressure transducer also attached to the catheter. Pulmonary capillary wedge pressure is a secondary measurement used in diagnosis and is measured by occluding small branches of pulmonary arterials with a balloon catheter to act as a surrogate measurement for the left ventricular end diastolic pressure (LVEDP) (Sharma 2013). Figure 2.2 on the following page shows a flow chart depiction of steps taking in diagnosing a patient with PH. Although this procedure is generally considered low risk, some of the potential complications involved with this procedure are bruising, excessive

bleeding (due to puncture), infection, formation of abnormal heart rhythms, clot formation and even possible rupture (Mayo 2015).

No studies could be found discussing compliance of patients to undergo this type of procedure; however, in Sharma 2013, of a total of 43 patients recommended to undergo a RHC, only 26 followed thru and underwent the treatment. This leaves roughly 40% of the studies population opting out of this invasive procedure.

While ECHO is the primary imaging technique used when initially diagnosing a patient with PH; previous studies have shown a correlation between the use of ECHO and the amounts of false diagnosis of PH in both the general population and various high risk populations; with false positive rates of roughly 36% in the general population (Badesch 2009) when compared to a final diagnosis through the, gold standard, highly invasive, use of RHC. Although the overall prevalence of PH in the general population is relatively low when compared to other high risk diseases, the amount of improper diagnoses and number of patients undergoing an unnecessary invasive RHC test, based off ECHO results, is what makes this a serious problem that needs to be addressed; along with developing a method to diagnose and study PH patients with an increase in accuracy and reduction in invasiveness. Some of the most common consequences resulting from PH are, right sided heart failure resulting from the heart overworking, trying to pump blood through blocked arteries, dilation of the pulmonary artery, arrhythmias, thickened artery walls, and blood clots (Mayo 2015).

2.3 MRI in PH

Over the years, MRI has further emerged as a tool to provide non-invasive prognoses in patients with PH. As far back as 1993, Boxt et. al. used MRI to quantify right ventricular volume in patients with PH. In this study the researchers were able to obtain tomographic images of the heart at multiple points in a cardiac cycle with the volume of the chamber itself being determined from the end-diastolic and end-systolic images (Boxt 1993).

Laffon et. al. described a method to noninvasively assess pulmonary hypertension using a MR phase-mapping method. In this method, both blood flow and PA cross sectional areas were collected through MRIs while pressures were gathered from RHCs. They were able to establish relationship between measured pressures and the MRI calculated pressures with a reliability of roughly 87% (Laffon 2001). In this study, they plotted pulmonary pressure measured from RHC versus pulse pressure, and RHC pulmonary pressure versus pressure wave velocity. They then used these two curves as limits to estimate pressures at varying pulmonary pressures and pressure wave velocity values.

Another study in 2011 by Barker et. al. conducted a multi-institution study assessing pulmonary artery flow and WSS in adults with PAH using both 4D and 3D flow acquisition. The study consisted of 19 healthy and 17 PAH subjects that underwent either a Cartesian 4D flow acquisition or a 3D radial acquisition. The study found an overall trend of a decrease in WSS in the PAH population versus the healthy (non-age

matched) control population. The PAH subjects had a combined average WSS in the MPA (averaged over the vessel circumference during systole) of 2.2 ± 1.0 dyn/cm^2 while the healthy population had a higher average at 4.0 ± 1.4 dyn/cm^2 in the MPA (Barker 2011); the averages in the LPA were 4.1 ± 0.18 dyn/cm^2 in healthy subjects and 1.6 ± 0.9 dyn/cm^2 in the PH population while the RPA were 5.4 ± 2.1 dyn/cm^2 in the healthy subjects and 1.9 ± 0.7 dyn/cm^2 in the PH subjects.

There have also been other attempts to calculate WSS from MRI data, through the use of a modified Poiseuille equation, as well as the "Ifrigg" method (Potters 2014, Iffrig 2015). Although Potters et. al. was investigating WSS in the aorta, intracranial aneurysms, and the carotid arteries, the basic idea of applying Poiseuille's equation to solve for WSS based on parameters obtained from MRI is still applicable to the pulmonary artery as long as the flow rate is obtainable through MRI. CFD is also emerging as a powerful tool in studying and quantifying disease progression.

2.4 Introduction to CFD

Computational Fluid Dynamics (CFD) is a set of numerical methods applied to obtain approximate solutions of problems of both fluid dynamics and heat transfer; in other words, a computer simulation for prediction of fluid-flow phenomena. The overall objective of CFD is to model continuous fluids with Partial Differential Equations (PDEs) and discretize PDEs into algebraic terms, in order to solve them. CFD aims to solve the following PDEs (Zikanov 2010):

$$\frac{\delta(\rho u)}{\delta x} + \frac{\delta(\rho v)}{\delta y} + \frac{\delta(\rho w)}{\delta z} = 0 \quad (2)$$

$$\rho\left(\frac{\delta u}{\delta t} + u\frac{\delta u}{\delta x} + v\frac{\delta u}{\delta y} + w\frac{\delta u}{\delta z}\right) = -\frac{\delta p}{\delta x} + \mu\left(\frac{\delta^2 u}{\delta x^2} + \frac{\delta^2 u}{\delta y^2} + \frac{\delta^2 u}{\delta z^2}\right) + \rho g_x$$

$$\rho\left(\frac{\delta v}{\delta t} + u\frac{\delta v}{\delta x} + v\frac{\delta v}{\delta y} + w\frac{\delta v}{\delta z}\right) = -\frac{\delta p}{\delta y} + \mu\left(\frac{\delta^2 v}{\delta x^2} + \frac{\delta^2 v}{\delta y^2} + \frac{\delta^2 v}{\delta z^2}\right) + \rho g_y \quad (3)$$

$$\rho\left(\frac{\delta w}{\delta t} + u\frac{\delta w}{\delta x} + v\frac{\delta w}{\delta y} + w\frac{\delta w}{\delta z}\right) = -\frac{\delta p}{\delta z} + \mu\left(\frac{\delta^2 w}{\delta x^2} + \frac{\delta^2 w}{\delta y^2} + \frac{\delta^2 w}{\delta z^2}\right) + \rho g_z$$

Where Equation 2 represents the continuity equation and Equation 3 represents the Navier-Stokes equations in the x, y, and z directions. The Navier-Stokes equations are a derivation of the concept of conservation of momentum, while the continuity equation is a derivation of the concept of conservation of mass. These equations assume a Newtonian fluid and incompressible flow. In these equations, p = pressure, ρ = density, μ = viscosity, and (u, v, w) = the velocity components. The pressure gradients, $\frac{\delta p}{\delta x}$, $\frac{\delta p}{\delta y}$, $\frac{\delta p}{\delta z}$, drive the fluid flow. The next term on the right-hand side represents the shear force for a Newtonian fluid. The last term on the right is the force due to gravity which was considered negligible in this study. The left side of the Navier-Stokes equation represents the mass times acceleration.

CFD based on MRI, has the ability to estimate hemodynamic metrics (wall shear stress, for example) of blood flow in the pulmonary arteries and has the potential to be a better screening tool for PH. Information gained and made available from computational analysis could also prove useful to study disease progression for post-treatment

assessment. Because an increase in pulmonary vascular resistance is a risk factor contributing to PAH, wall shear stress should decrease with the increased vascular resistance and could potentially be detected prior to significant measurable increases in PA pressures (Kheyfets 2013). The use of CFD to noninvasively assess the severity of PH and gauge response to PH-specific treatments has the potential to significantly revolutionize clinical practice in this field.

The following steps demonstrate the necessary procedure taken in order to successfully solve a problem using CFD. First, a geometry description is developed (what part of the body/object is being investigated). Next, the imaging and segmentation of the geometry is conducted, followed by the meshing of the geometry. Boundary conditions and specific flow conditions and properties are applied before the solver settings are finalized and a solution is generated. Lastly, any post processing is conducted including the analysis and visualization of the results.

2.4.1 Imaging

Depending on the flow information required, hemodynamics in the pulmonary system can be simulated in either two or three dimensions. While two-dimensional analysis can incorporate patient-specific anatomical metrics and can accurately reveal general physiological flow conditions, while at the same time being fairly inexpensive and easy to compute; three-dimensional flow simulations reveal in greater detail the flow dynamics in the PA, although at an increased expense in the form of computational cost and time (Formaggia 2003, Olufsen 2000).

The basis for conducting the three dimensional CFD simulations begins with reconstructing the computational domain from thoracic computed tomography (CT) or magnetic resonance (MR) images (Vignon 2010). In order to use numerical simulations with these images, preprocessing must be conducted to eliminate “non-anatomical” surface features, adding inlet and outlet extensions, while also dividing the geometry into subdomains, meshing, in order to solve the numerical continuity and momentum equations (i.e. Navier Stokes Equations).

As mentioned before, clinical images that reveal the structure of the vasculature can be obtained using volumetric CT or MRI without a contrast agent, although contrast-enhanced images are often preferred whenever available for better reconstruction accuracy (Vignon 2010). Figure 2.2 on the following page shows an example of an MRI taken that could be used to develop a 3D model of the pulmonary artery. In the figure, the main pulmonary artery (MPA), right pulmonary artery (RPA), and left pulmonary artery (LPA) can be seen.

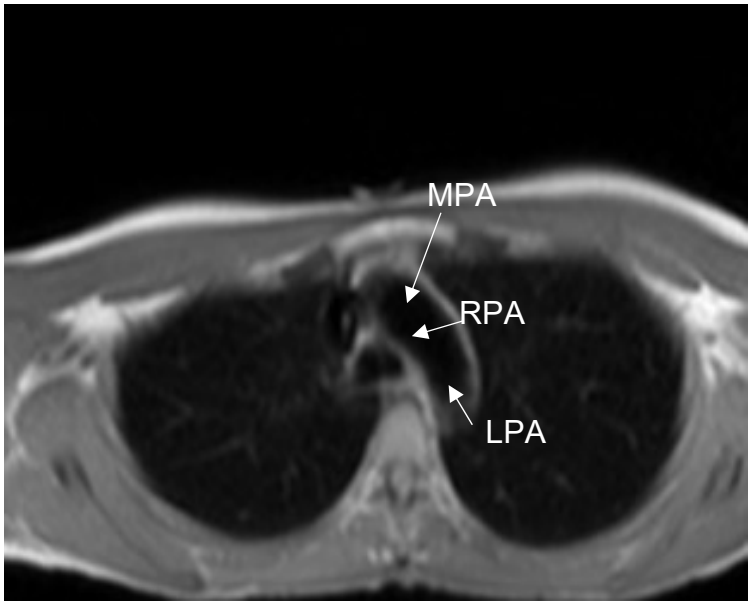

Figure 2.2 MRI Cross Section Showing main, left, and right pulmonary artery (MPA, LPA, and RPA)

2.4.2 Phase Contrast MRI

PC-MRI, also known as a Phase Contrast MRI, is a way to non-invasively, accurately measure flow with both spatial and temporal resolution (Lotz, 2002). Using the subject's PC-MRI's allows for patient specific flow parameters (velocity, mass flow rate) to be used as boundary conditions in CFD simulations.

2.4.3 Segmentation

In order to run the simulations, the MRIs for both geometry creation and velocity calculations require segmentation. Segmentation is the process by which pixels in the image are labeled as part of the connected vascular network, distinct from the lungs or

surrounding anatomical features (heart, chest wall, diaphragm, pulmonary tumors, etc.). In order for a segmentation method to be considered “successful” it must not only reconstruct key anatomical structures but also separate the arterial system from the venous system (Vignon 2010). Historically, manual segmentation of the vascular tree is considered the gold standard, but this is time consuming and labor intensive, making clinical implementation impractical (Kheyfets 2013).

Many existing partially or fully automated methods can rapidly reconstruct the pulmonary vascular system to a large number of generations (Ebrahimdoost 2011), but most are susceptible to discontinuity artifacts present in the imaging methods and are unable to reveal both distal and proximal vasculature. Burrowes et al. (Burrowes 2005) showed a novel technique for reconstructing a continuous 3D model of the pulmonary system all the way to the terminal bronchioles. In Burrowes’ study, X-ray computed tomography along with a contrasting agent was used to image and visualize the vasculature up to 2,500 vessels per model. Finally, due to the complexity of the resulting vascular networks none of the methods are “automatic” and do require significant manually intensive efforts for calculations to be conducted, the available techniques are not yet suitable for directly implementing 3D CFD analysis in a clinical setting; however, if implemented with other segmentation methods, in the future this could possibly be used for rapid patient vasculature modeling (Ebrahimdoost 2011). In addition, none of the automated segmentation techniques being able to be applied in a clinical setting, by either sending results to a lab to generate CFD results or having the capability of running CFD simulations in an operating room immediately after

undergoing an MRI, none of the currently researched methods have been validated in real time while directly monitoring pulmonary arterial metrics (Kheyfets 2013). Being able to do this in real time can help to more quickly diagnose PH while eliminating the traditional invasive diagnostic methods.

For three-dimensional flow analysis, the current “semiautomatic” segmentation methods currently available, are the most practical options. Semiautomatic segmentation of the pulmonary vasculature can be done with commercial software; Mimics, 3D Slicer, ImageJ, ITK Snap are all examples of free commercially available software that can segment CT/MRIs. Initially, thresholding is used to identify all vasculature within the CT or MRI image sequences (Burrowes 2005). After thresholding, artery isolation can be accomplished using region growing algorithms and recognizing that arterial vessels are always accompanied by airways (Burrowes 2005). Once the 3D geometries are recreated through segmentation, a computational mesh needs to be generated in order to run the CFD simulations.

2.4.4 Meshing

The computational domain must be divided into a finite number of elements to discretize and solve both continuity and Navier Stokes equations (Spiegel 2001, Tu 2008). The mesh must resolve the complex geometry of the pulmonary vasculature while also being dense enough to analyze the physiological flow dynamics. Anatomical computational domains can be discretized using tetrahedral (Prakash 2001) or sometimes hybrid (Bove 2003) meshes. A mesh independence study needs to be

conducted with increasing mesh densities to ensure that the solution generated is no longer affected by the mesh density. Once the mesh is generated, the models are ready to be imported into the solver and have boundary conditions applied.

2.5 Introduction to Boundary Conditions

Since it is essentially impossible to account for every single condition that could affect a solution, boundary conditions are applied to CFD problems to account for certain assumptions to simplify the problem being solved. For example, in the case of a pulmonary artery, one can apply that the relatively cylindrical vessel being studied is made of rigid walls and have a no slip condition at the walls of the vessel. Whether the fluid being investigated is inviscid or viscous, or if the flow is steady or unsteady, all of these types of conditions need to be specified in order to generate an accurate solution. If the computational domain has open boundaries (i.e. inlet or outlet) boundary conditions need to be applied for these zones as well.

2.5.1 Inlet Boundary Conditions

Overall, there are many different types of boundary conditions that can be applied to inlets. Mass flow, velocity, pressure, inflow, inlet vent/fan type conditions can all be applied to inlets when conducting CFD. For use with incompressible flows the use of either a pressure inlet or velocity inlet will provide the best results, while for compressible flow an inflow or mass flow inlet boundary condition would be more appropriate.

When modeling flow in a pulmonary artery, a fully developed inflow velocity profile can reduce inconsistencies between physiological (in-vivo) and CFD calculated flows (Kheyfets 2013); this can be obtained by extending the inlets to allow enough time for the flow to become fully developed. Patient-specific inlet waveforms can be obtained through invasive right heart catheterization, as discussed above, or if pressure is not required, transthoracic echocardiography (TTE) or MRI with phase-contrast (PC-MRI) for velocity encoding (Kauczor 2009). Using the Womersley solution, a velocity is able to be calculated as a function of time and radial coordinate location within a cross section (Womersley 1955). This method is intended for use in a perfectly cylindrical tube section, however, the PA is not perfectly cylindrical; using Schwarz-Christoffel (SC) mapping, a cross section can be mapped using only the relevant anatomical information as close to a perfect circle as possible (Boutsianis 2008). This method can also be used to apply experimentally flow conditions on the reconstructed geometry involved in CFD applications.

2.5.2 Outlet Boundary Conditions

As with inlet boundary conditions, varying circumstances require the use of varying boundary conditions. In the case of incompressible flow, a pressure outlet or outflow boundary condition should be used, whereas compressible flow allows the use of mass flow outlet or a pressure based outlet. The use of an outflow or pressure outlet condition would be most appropriate for studies looking at the pulmonary artery.

Another option for an outflow boundary condition is to set each outlet pressure to a constant value, which can result in non-physiological flow within the computational domain because the flow split is entirely governed by the vascular geometry (Vignon 2006). A three-element Windkessel outflow boundary condition is a lumped model that accounts for the resistance and compliance of the distal vasculature (Kung 2011).

2.6 Solver Preferences

After applying appropriate boundary conditions for the problem being solved, solver settings also need to be applied. In most cases, there are two primary solver settings, a pressure based and density based solver. A pressure based solver uses momentum and pressure as the primary variables and is used in a wide range of flow schemes including incompressible low speed flows (flow in the Pulmonary Artery). While a density based solver uses vector formation and is typically used for problems that show interdependence between variables (hypersonic flows/shock interactions). Included in the solver preferences are any fluid properties necessary to develop an accurate solution, including viscosity, density, and temperature. Because the solutions generated through CFD are not exact solutions, convergence needs to be reached. Convergence, often measured by the level of residuals, the amount by which discretized equations are not satisfied, and not by the error in the solution, is used when it is necessary to be sufficiently close to the solution for a particular required level of accuracy.

2.7 CFD Parameters

Multiple parameters can be used to quantify the hemodynamics in the pulmonary circulation. However, possibly the most important metric studied is wall shear stress (WSS), where WSS in this case is the tangential drag force produced by blood moving across the endothelial surface, as it is the greatest contributor to vascular homeostasis (Kheyfets 2013). The arterial wall will gradually increase lumen diameter in response to increased pressure in an effort to normalize physiological WSS (Zarins 1987). For clinical applications, since the WSS is typically available through noninvasive measurements, it would be useful to correlate these values and compare with the previously discussed metrics used to assess PH disease progression, currently obtained through invasive and expensive catheterization.

With CFD you are able to generate various types of plots or models to visualize the solutions to problems. Contour plots of velocity, pressures, WSS (to name a few) can all be generated. Fluent calculates WSS using the following Equation 4 below:

$$\tau_w = \mu \frac{\delta v}{\delta n} \tag{4}$$

Where the WSS (τ_w) is equal to the viscosity times the partial differential of the tangential velocity normal to the boundary wall. The above equation assumes a Newtonian fluid. CFD has been emerging as a powerful tool to non-invasively monitor or evaluate disease progression and in more recent years has expanded to the pulmonary artery. CFD programs also allow the use of particle tracking to see areas of fluid recirculation in a specific geometry.

2.8 Current Pulmonary Artery CFD Models

Tang et al. developed a 3D finite element CFD model of the pulmonary vasculature to examine the impact of exercise on arterial hemodynamics. The arteries were reconstructed based on lumen topology for large vessels and assumed to be circular for smaller vessels. They used a pressure based outflow boundary condition to investigate shear stress distributions, and energy dissipation in six subjects. Resistance values at each outlet were assigned based on vessel diameter at the outlets and were adjusted for each patient to agree with MRI-measured flow split and total vascular resistances. The study found that exercise increases mean WSS and decreases energy efficiency (Tang 2011). Figure 2.3 shows the wall shear stress distribution found in the study. In the figure, there is a clear increase in the overall WSS after exercise compared to before exercise, along with these changes appearing to be more proximal than distal. There were more portions of the pulmonary artery at the maximum 35 dyn/cm^2 post exercise than before, even in the proximal arteries where the WSS was typically closer to 0 dyn/cm^2 at rest and during diastole.

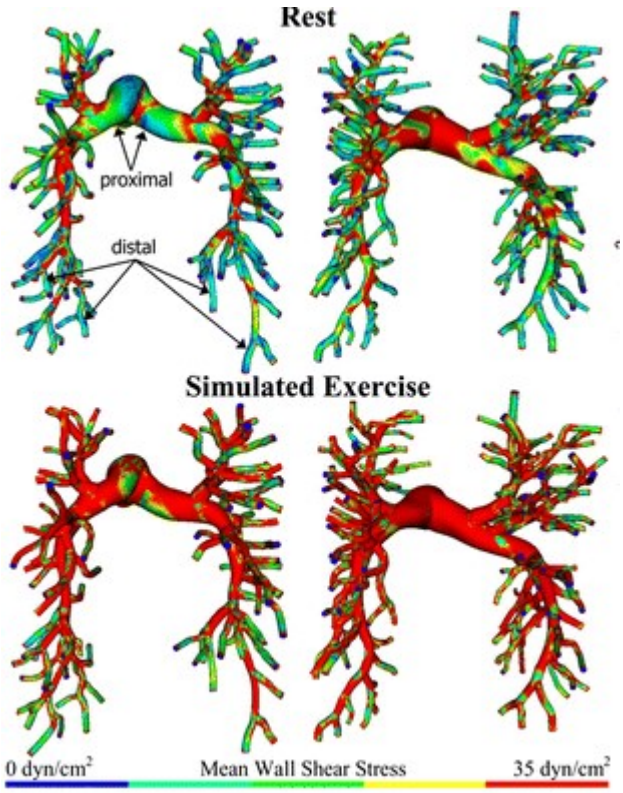

Figure 2.3 Wall Shear Stress Distributions Before and After Exercise (Tang 2011)

Tang also published a second paper in 2012 using CFD and suggesting that WSS is lowered in subjects with pulmonary hypertension. Using MRI derived geometries and CFD an automatic mesh was generated using a commercially available program known as “MeshSim”; velocity inlet boundary conditions along with pressure outlet boundary conditions were assumed. Along with these, the walls were assumed to be rigid with no slip conditions at the wall. This study demonstrated the first time 3-D hemodynamic conditions were used to quantify parameters in patient specific models of Group 1 PH Figure 2.4 represents a time averaged wall shear stress contour map of both a healthy and PAH diseased pulmonary artery. A clear decrease in wall shear stress is seen in the PAH artery (Tang 2012). The WSS was averaged over 10mm strips in both the left

and right pulmonary artery, averaging 20.5 ± 4.0 dynes/cm^2 in the proximal arteries for the normal subjects and 4.3 ± 2.8 dyn/cm^2 in the PAH subjects (Tang 2012).

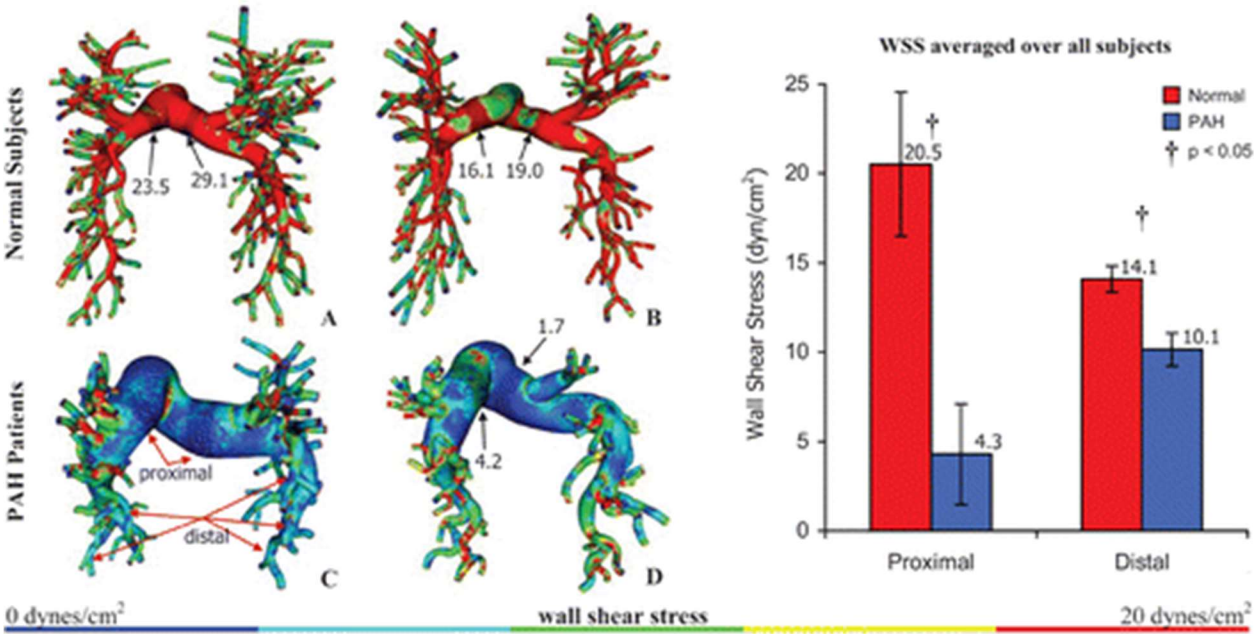

Figure 2.4 Time Averaged Wall Shear Stress in Both a Healthy and PAH diseased Pulmonary Artery (Tang 2012)

Kheyfets et al, also looked to develop patient specific models of blood flow in the pulmonary circulation within a PH population. This study was aimed at determining the effects, varying outlet conditions had on patient specific results. They were able to conclude that implementing generic outflow boundary conditions still resulted in statistically significant WSS values suggesting that the CFD model could be executed without the need for complex outflow boundary conditions that require invasively obtained patient-specific data (Kheyfets 2015). One of the primary limitations dictated by the authors was the lack of any validation methods for their results as there were no MRIs conducted to be able to compare their results to. Figure 2.5 on the following page represents a WSS contour for one of their subjects which clearly shows an increase in

WSS immediately following the initial split into the LPA and RPA as well as a maximum of roughly 50 dyn/cm^2 near the outlets.

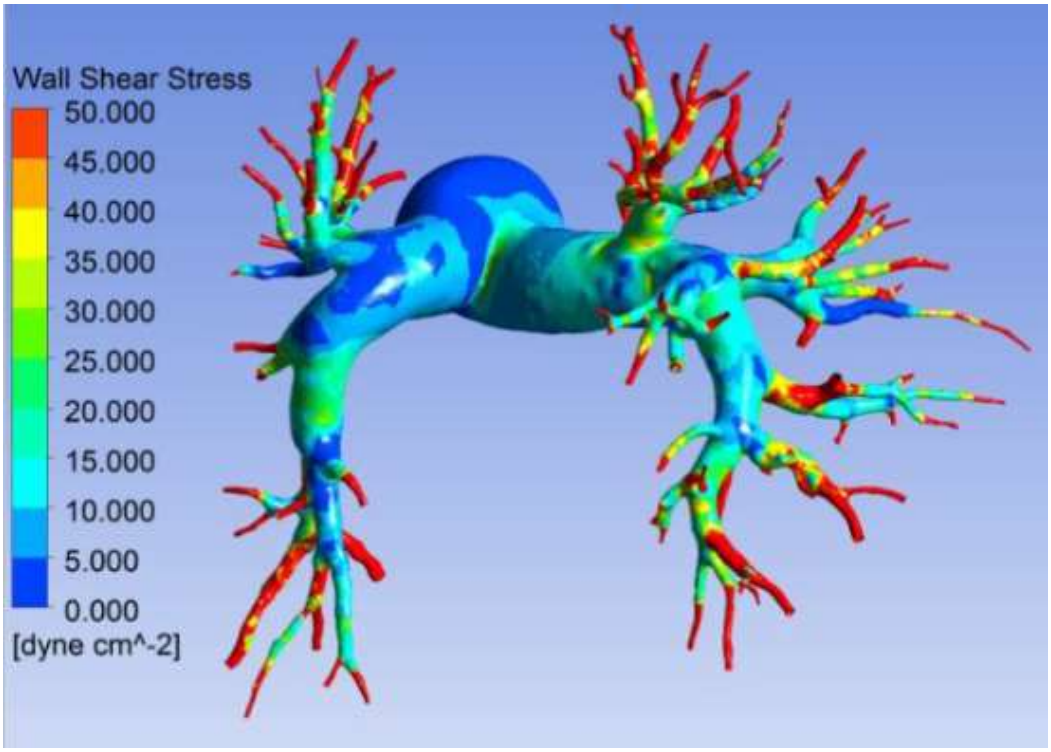

Figure 2.5 WSS Contour Map of PH Subject (Kheyfets, 2015)

CFD work has also been done in pediatric patient specific PA's (Hunter 2006), as well as pulmonary hemodynamics being modeled to gain insight into multiple pathologies such as pediatric pulmonary hypertension (Hunter 2010, 2008) and pneumothorax (Christophe 2012).

To summarize, work has been done in this field with using MRI alone to calculate WSS values in a PH population (Barker 2011). There have been attempts to conduct CFD using CT scans to generate the 3D models and a finite element solver to gather computational results in both a healthy and PAH population (Tang 2012). And there

have been attempts using CT scans coupled with a finite volume based solver to determine the effects of outlet boundary conditions on results (Kheyfets 2015). This current study uses MRI rather than CT scans as well as a different type of solver. Tang et. al. used a finite element solver with a parabolic flow profile versus a finite volume solver and blunt flow profile being used in this study. This study was done in an attempt to quantify in a similar fashion, changes in hemodynamics between a healthy and PH population with slightly altered methods.

CHAPTER 3

METHODS

3.1 Experimental Methods

3.1.1 Subject Selection

A total of 20 subjects have been recruited for this study. Their MRIs were collected over 2011-2017, and all MRIs were conducted at Vidant Medical Center's MRI clinic. Subjects who had elevated sPAPs (based on TRV) on ECHO and subsequently had a RHC were invited to participate in this study. Control subjects were invited to participate if they tested negative on their ECHOs, and therefore did not have a RHC. It should be noted that this study has been approved by the Institutional Review Board (IRB) of East Carolina University, UMCIRB 11-0275 "Investigation of Pulmonary Artery Hypertension Using MRI and Computational Fluid Dynamics". Of the 20 subjects recruited, only four subject's data were included in this subproject due to limited inclusion of the pulmonary branches in the anatomy MR scans for the majority of the subjects.

3.1.2 Clinical Data

Table 3.1, containing a summary of the subject information as well as data collected from the RHCs, can be seen on the following page; the echocardiogram and RHC were done as routine standard of care for the patients. Of the four subjects studied, 3 were female and one was male, with ages ranging from 32-64 years old. There was one control subject and three PAH subjects. Subjects 14 (control) and 16 had sickle cell

disease. It should be noted that a mPAP > 25 mmHg is representative of PH while a PVR typically less than 1.6 woods units is considered healthy. All three PAH subjects had a mPAP well above the 25-mmHg diagnostic mark as well as 17 and 18 having unhealthy PVR values.

Table 3.1 Summary of patient data including information from RHCs. mPAP (mean Pulmonary Arterial Pressure); sPAP (systolic Pulmonary Arterial Pressure); PVR (Pulmonary Vascular Resistance); PCWP (Pulmonary Capillary Wedge Pressure)

Subject	Age	Sex	PAH or PVH	mPAP (mmHg)	sPAP (mmHg)	PVR (Woods Units)	PCWP (mmHg)
14	36	F	Control	n/a	n/a	n/a	n/a
16	44	F	PAH	38	49	0.87	n/a
17	32	F	PAH	45	70	7.18	7
18	64	M	PAH	38	53	13.9	6

3.1.3 Image Acquisition

Two different image sets were used for each patient, in regards to the geometry recreation and the velocity profile creation. All images were gathered on a Siemens Espree (subject 14) 1.5 T or Siemens Aera 1.5 T model MR scanner (subjects 16, 17, and 18). The sequence used for the geometry images was a gradient echo (GR) sequence. This type of MR sequencing is commonly used when fast imaging is important, as it is in this application of a cardiac MRI. This sequence uses a fully balanced gradient waveform that allows this sequencing method to be relatively reliable even in subjects who have difficulty holding their breath for extended periods of time. The scans were conducted without the addition of a contrasting agent; acquired by the subjects lying in the supine position under breath hold conditions. The intent was to capture the PA from the left ventricle outflow track through the left and

right PA branches. Slice thickness was 3.5 (subject 14) to 6.5 mm (subjects 16, 17, 18) mm with no gaps between the slices; this allowed 17-25 slices to be generated per subject. Other scan parameters included an echo time of 2.9 ms to 3.26 ms and a repetition time of 0.126 ms to 0.13 ms. The pixel spacing ranged from 1.69 mm to 1.92 mm. Some of the above parameters varied between subjects based on the date the scans were completed, who conducted the scans, and the patient's anatomy.

PCMRI scans were used to measure and calculate area and velocity changes over the cardiac cycle. PCMRI is an imaging technique that is used to visualize moving fluids; using this type of MRI you are able to determine the velocity of a fluid by quantifying the phase shift of a moving spin, which is proportional to its velocity. The images were acquired by the subjects lying in the supine position and under breath hold conditions. Data was collected in the PA just past the leaflets, the mid-PA, the LPA and the RPA. Slice thickness was 6 mm for all subjects with no gaps between the slices; this allowed thirty images to be generated for each subject totaling to one full cardiac cycle. Other scan parameters included an echo time of 2.81 ms to 3.22 ms and a repetition time of 0.408 ms to 0.429 ms. The pixel spacing ranged from 1.76 mm to 2.08 mm. The velocity encoding number (V_{enc}) varied from 90-150 cm/s; however, for most images evaluated the V_{enc} was 90 cm/s. The V_{enc} is representative of the maximum velocity expected to be encountered in the vessel being investigated and is used in the conversion of image intensity to velocity.

3.1.4 MRI Velocity Data Processing

All MATLAB codes used in the MRI data processing were developed by past lab students (George 2014, George 2012). First, a code was used to crop the PA to isolate it from other sections of imaged vasculature. Next, the PA images were segmented using a separate MATLAB code utilizing region-growing methods. Manual corrections to the segmented images were sometimes needed to acquire the proper PA area. The area was segmented for each of the 30 total time points per cardiac cycle, to allow for measurement of area change over time. The last code used took the segmented image of the PA, and multiplied it with the phase portion of the image to obtain the velocity in the region of interest. From this code, the velocity, flow rate, diameter, and area of the PA images could be calculated.

3.1.5 MRI WSS Calculations

WSS can be estimated from a modified Poiseuille's equation seen in Equation 5 below:

$$WSS = \frac{4\mu Q}{\pi r^3} \quad (5)$$

Where μ is equal to the viscosity, Q is equal to the flow rate and r is equal to the radius of the vessel in question. Using the flow rate at peak systole and radius information determined from the MRI's as well as the viscosity of blood allows an estimation of WSS to be calculated. This equation however assumes the following: the fluid is incompressible and Newtonian, and the flow is laminar.

3.2 Numerical Methods

3.2.1 Geometry Creation

Upon retrieval of these patient's confidential MRIs from Vidant Medical patient specific geometries were recreated using the 3D segmenting software Mimics (Materialise, Inc., Plymouth, MI). Figure 3.1 below shows both an original MRI slice from subject 14's MPA (left) and a thresholded image of the same slice (right).

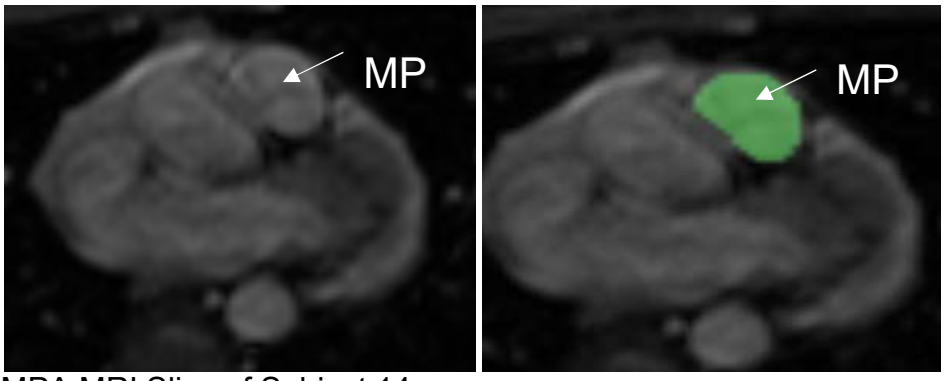

Figure 3.1 MPA MRI Slice of Subject 14

The following segmentation steps were followed: First, a contrast was applied with the "windowing" command; this highlights any specific tissue with varying intensities for bone, soft tissue, fatty tissue, skin tissue, composite bone, or spongial bone. Next, a thresholding command was used which eliminated regions with intensities below the set threshold level. Manual editing was conducted to ensure only the PA was selected. This thresholding process was continued over multiple slices, varying between subjects, before being combined and smoothed into a 3D model. After segmentation, the slices were verified by a Cardiologist at ECU's Brody School of Medicine. Figure 3.2 below shows the 3D model of Subject 14 post smoothing. Smoothing was conducted in mimics using the "Smoothing" command over a set number of iterations (dependent on the subject) until the model appeared visually smooth. The models generated through

Mimics were then imported into SolidWorks (Dassault Systemes, Waltham, MA) as a .STL file in order to perform necessary post-processing of the model before mesh generation.

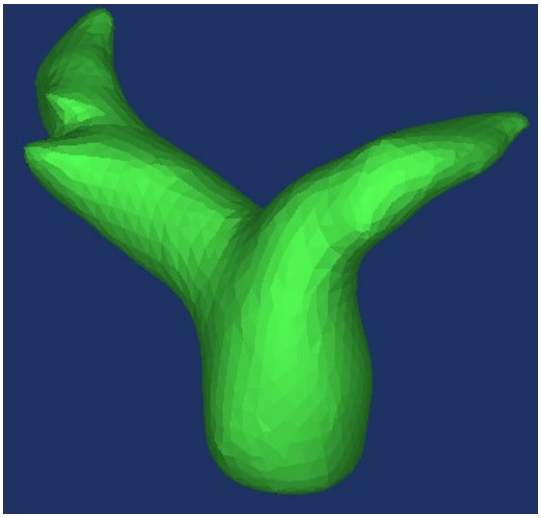

Figure 3.2 Example of 3D Model generated in Mimics, post smoothing

3.2.2 Geometry Post Processing

The models generated through Mimics were then imported into SolidWorks (Dassault Systemes, Waltham, MA) as a .STL file in order to perform necessary post-processing of the model before mesh generation. Once in SolidWorks, the inlets and outlets were cropped perpendicular to the long axis of the vessel and at a location that ensured the diameter of the vessel was preserved. The boundary conditions for the simulations will be applied to these cut surfaces.

3.2.3 Meshing

The completed solid models were then imported into ANSYS Workbench (ANSYS, Inc., Canonsburg, PA) in order to generate the computational mesh needed to perform the

CFD calculations. An average of approximately 1.3 million tetrahedral mesh elements were needed for each model. Table 7.1 in Appendix A summarizes the mesh metrics for all subjects including number of elements and the overall quality of the meshes, based on Fluent's built in mesh quality scales. Final geometries as well as images of the meshes used for each subject can be found in Appendix A: Figures 7.1-7.4. The mesh density near the vessel walls was also changed, by prescribing inflation growth ratios of 1.0 to 1.5; increasing this growth ratio reduces the total height of the inflation layer, reducing the sizing of the inflation elements nearest the boundary. This allows for a more accurate calculation of WSS since it is based on velocity near the wall. The final mesh densities can be seen in Appendix A: (Table 7.8), as well as a cross section of one of the meshes shown below in Figure 3.3.

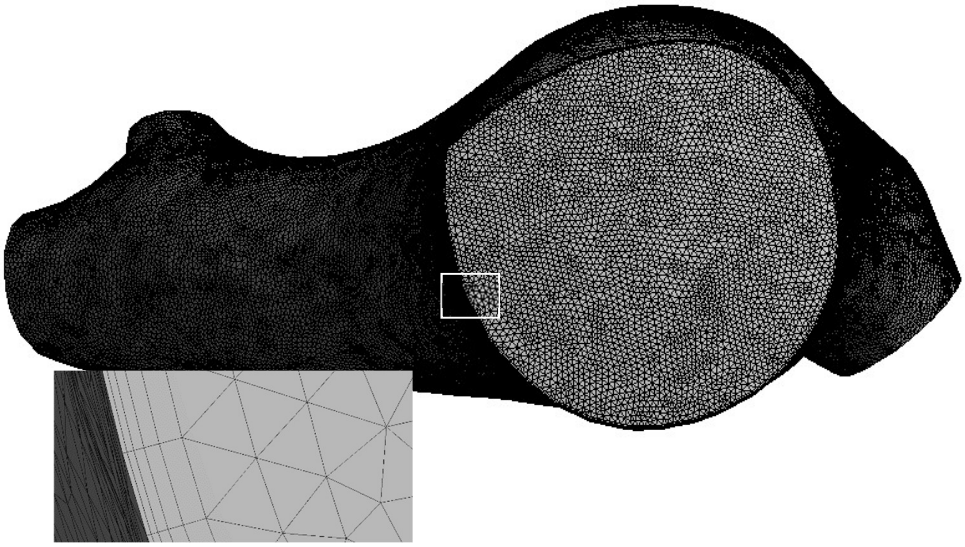

Figure 3.3 Cross Sectional View of Mesh Density (post increasing density near the wall)

3.2.4 Mesh Independence

Upon convergence of the initial mesh size, a Mesh independence test was conducted to ensure the results are accurate in relation to changes in the mesh sizing. Table 7.2 in

the Appendix A summarizes the varying mesh inputs used to develop equivalent mesh sizes differing only by the size of the subjects individual PA sizes; these were used to run multiple simulations in order to achieve mesh independence.

Using the inputs from Table 7.2, four different mesh sizes were developed for each model. These were all run through the same simulation setup described above and the max velocity at peak systole was compared between the trials in order to determine whether the number of mesh elements (mesh density) had an impact on the results. The mesh was deemed "fine" enough when there was less than a 1% difference between the max velocity values at peak systole of each subject's cardiac cycles. For all models the finest sized mesh was used for all final results and calculations. This leaves a total of eight meshes being used; four pre-increasing mesh density near the wall and four post-increasing mesh density near the wall. The test information can be seen summarized in Appendix A: Table 7.3.

3.3 Boundary Conditions and Fluid Properties

The properties of the media (blood) were input into FLUENT which included a viscosity (3.2 cP) and density (1,060 kg/m^3). A no-slip condition was also applied to the walls of the vessel. A velocity inlet condition was used with a blunt flow profile representative of a full cardiac cycle being used to simulate pulsatile flow; this flow information was calculated from the patient specific MRIs using MATLAB. MR calculated flow rates were fit to the model dimensions and a user defined function (UDF) containing the pulsatile velocity waveform over three cardiac cycles was developed for each subject.

The MATLAB code interpolated between the MR derived values to decrease the simulation time step. UDF's are used when the Fluent's settings need to be customized in a way not possible by altering the basic settings. Lastly, pressure outlet conditions were used with pressure set to 0 gauge.

3.4 Running the Simulations

3.4.1 Solver Preferences

The solver settings were defined as a second order pressure based solver, with transient flow, in order to accurately simulate multiple cardiac cycles; due to the relative simplicity of the geometry being studied, a more complicated solver was not deemed necessary to provide accurate results. The time steps for each subject were calculated by multiplying the RR interval (time for one cardiac cycle) of each subject by three, in order to represent three cardiac cycles. This number was then divided by the total number of velocity inputs for each subject. For subject 14, there were 4500 velocity inputs with an MRI calculated velocity every 50 time points; however, due to computational time, it was found that by reducing the velocity inputs to only 180 per subject (with an MRI calculated velocity every 2 time points) computational time was reduced while not affecting the results. Three cycles were used to limit any initial starting effects of the simulations.

3.4.2 Convergence

The simulations were run for an appropriate number of iterations per time step in order to allow convergence at each time step. Solutions were converged, and deemed

acceptable, when the residuals reached a value of 10^{-4} or lower. Simultaneously, a surface monitor was implemented to ensure the velocity magnitude at the inlet was corresponding to the correct input velocity values. This can be pictured for Subject 16 in Figure 3.4 below. It should be noted that the surface monitor from Fluent only plots the velocity magnitude. However, because some of the actual velocity data was negative (representative of reversed flow), in order to produce a similar plot based on the input velocity values from the patient specific MRIs it was necessary to calculate the absolute value of all the inputs to plot the velocity magnitude for comparison. Along with monitoring the inlet conditions, the mass flow rate at the inlet and outlets of each model was monitored to ensure conservation of mass throughout the simulations.

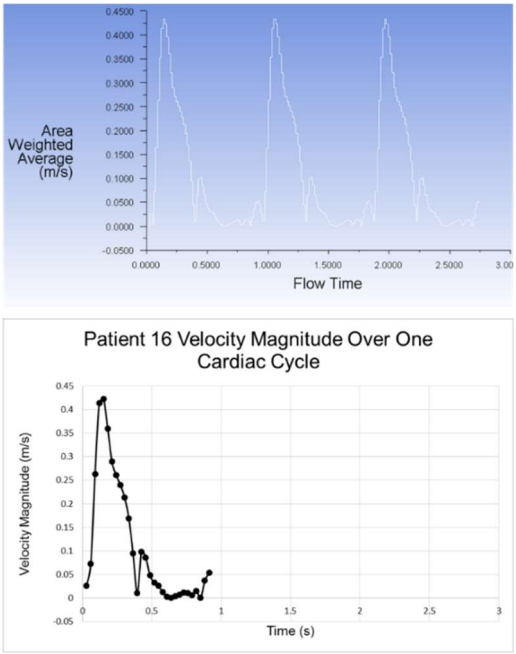

Figure 3.4 Comparison between Fluent's surface monitor of velocity magnitude at the inlet (top) vs. MRI calculated velocity magnitude at the inlet (bottom).

3.5 Post Processing

All post-processing including contours of WSS, velocity, as well as volume rendered velocity plots throughout the entire geometry for each model was completed in CFD-Post (ANSYS, Inc., Canonsburg, PA).

3.6 Validation

In order to validate the results, velocity contours at both the mid main pulmonary artery (subject 16 and 18) and left pulmonary branch (subject 14 and 17) were compared between the CFD data and the MRI processed data to assess whether the CFD is producing similar velocity profiles as well as flow patterns when compared to the real, MRI flow data.

CHAPTER 4
RESULTS

4.1 MRI Velocity Results

This section compiles all of the velocity data generated through MATLAB calculations of the MRIs. The data was measured just past the leaflets and represent the flow rate used to generate the BC's. Data in Table 4.1 includes time-averages of the area, velocity, flow rate, and diameter. The flow rate along with the area of the inlet calculated from the CFD model was used to calculate a velocity waveform that was applied to the CFD inlet. These final velocities can be seen in Appendix A: Tables 7.4-7.7 and also plotted as a function of time in Figures 4.1 to 4.4.

Table 4.1 Summary of MRI Calculated Data (Averages)

Subject	Area (cm^2)	Velocity (cm/s)	Flow Rate (ml/min)	Diameter (cm)	Max WSS (dyn/cm^2)
14	5.70	13.95	4770	2.69	5.400
16	12.76	8.02	6143	4.03	2.839
17	10.29	3.93	2425	3.62	1.347
18	10.06	3.49	2106	3.58	1.177

The average area of the PAH subjects (16, 17, and 18) inlets were roughly double that of the control subject while the velocities measured through MRI were approximately one half to one third that of the control subject. Using the modified Poiseuille's equation the WSS (last column in Table 4.1) was calculated at peak systole for each subject and the max WSS ranged from 1.177 dyn/cm^2 to 5.400 dyn/cm^2.

4.2 Validation Results

Figures 4.1-4.4 below depict the results from the validation completed. MR-derived velocity magnitude at either the middle of the MPA (subjects 16 and 18) or at the middle of the LPA (subjects 14 and 17) was compared to the velocity magnitude from the CFD simulations at the same location.

The figures show the CFD calculated velocity magnitudes (left) compared to the MRI calculated velocity magnitudes (right). The timing of these images is depicted in the velocity waveform (obtained from MRI) at the bottom of each figure, showing the location in each cardiac cycle. Location A is early systole, location B is peak systole and location C is the start of diastole. These three time points were used in an effort to get a varying range of flow conditions in the PA. Overall, the results are validated however there some discrepancies between the CFD and MR values which will be analyzed in the discussion section.

Figure 4.1 on the following page represents the validation results for subject 14. The CFD results are shown on the left while the MRI results are shown on the right. One validation slice from the middle of the LPA was used. Although the peak velocities with subject 14 varied (1.8304 m/s from CFD to 0.6 m/s from MRI data, qualitatively the peaks are happening on the same side of the vessel in a relatively similar pattern. There was a random “blip” of lower velocity in the MRI data during peak systole.

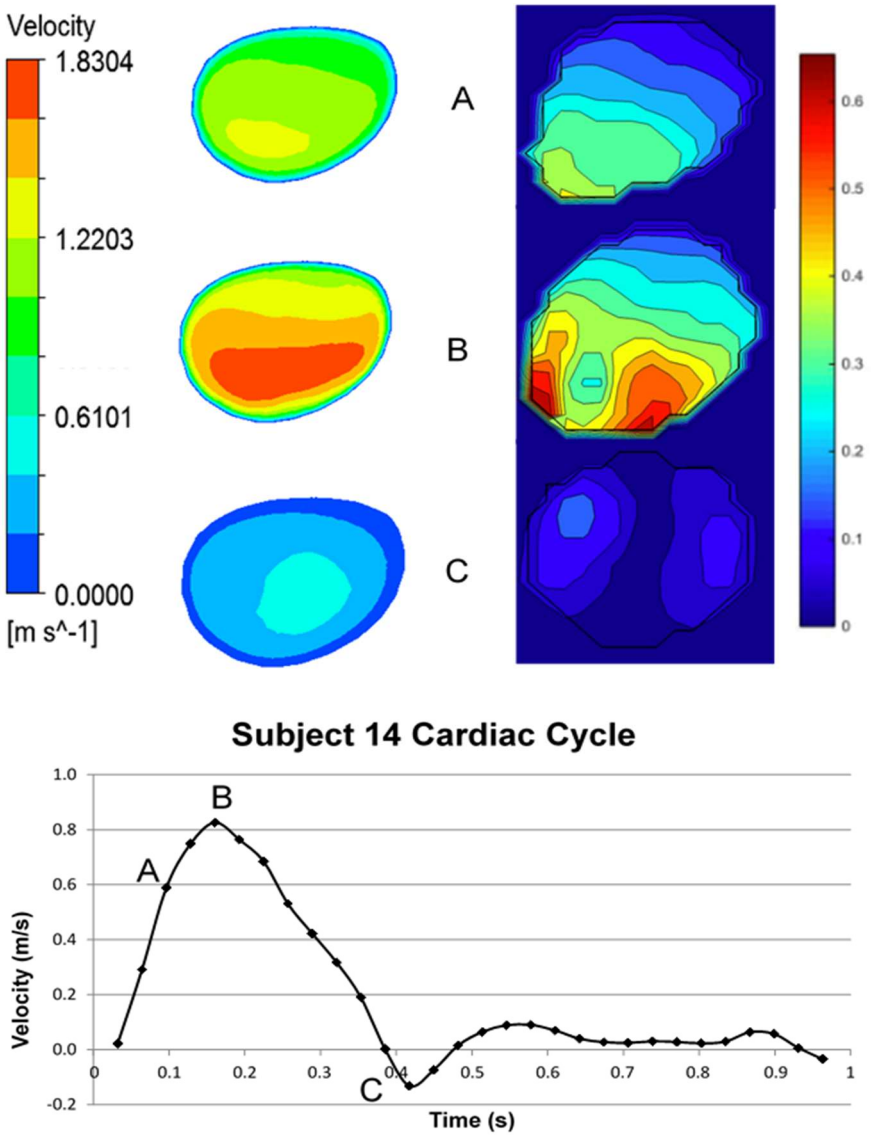

Figure 4.1 Validation of Subject 14 Simulations Using MRI velocities in m/s from the mid plane of the LPA. For the CFD simulations (Left) and MRI (Right). The bottom image represents a visualization of the velocity over time calculated from the MRI sets. The velocity is from the inlet and this is only being used as a representation of time.

Figure 4.2 on the following page represents the validation results for subject 16. The CFD results are shown on the left while the MRI results are shown on the right. One validation slice from the middle of the MPA was used. Although the peak velocities with subject 16 varied (0.7231 m/s from CFD to 0.6 m/s from MRI data, qualitatively the

peaks are occurring in the same location of the vessels cross section side. Also, the same swirling type velocity formation can be seen in diastole in both models. The velocity values for this subject were much closer quantitatively than the control subject, only differing by a tenth, and qualitatively, there wasn't the random "blip" at peak systole.

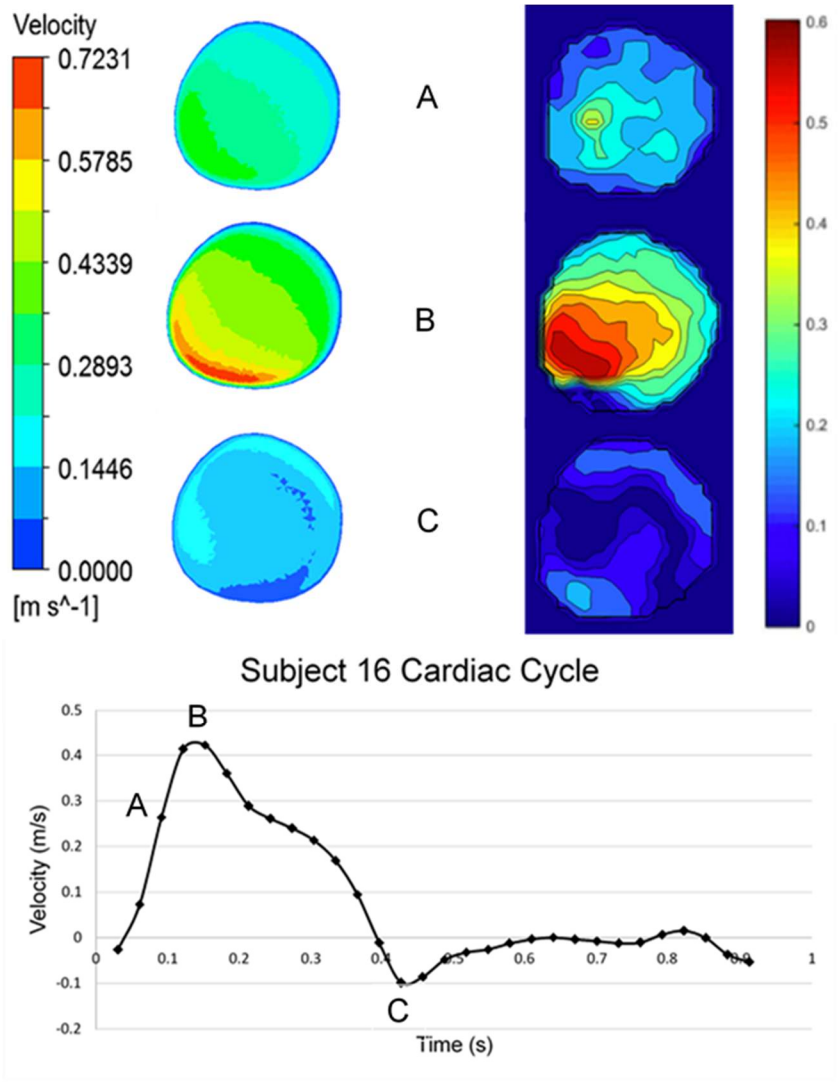

Figure 4.2 Validation of Subject 16 Simulations Using MRI velocities in m/s from the mid plane of the MPA. For the CFD simulations (Left) and MRI (Right). The bottom image represents a visualization of velocity over time calculated from the MRI sets. The velocity is from the inlet and this is only being used as a representation of time.

Figure 4.3 on the following page represents the validation results for subject 17. The CFD results are shown on the left while the MRI results are shown on the right. One validation slice from the middle of the LPA. Although the peak velocities with subject 17 varied (0.5448 m/s from CFD to 0.25 m/s from MRI data, qualitatively the peaks are happening on the same side of the vessel in a relatively similar pattern. Also, the same swirling type velocity formation can be seen in diastole (C) in both models. The velocity values for this subject were much closer quantitatively, only differing by tenths, and qualitatively, there wasn't the random "blip" at peak systole.

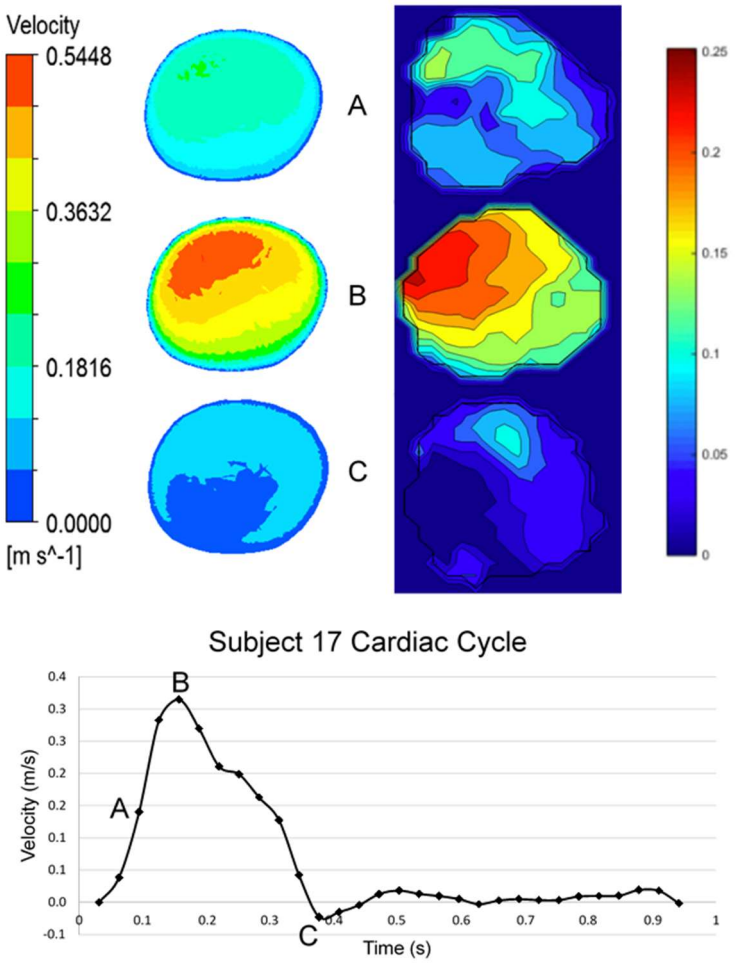

Figure 4.3 Validation of Subject 17 Simulations Using MRI velocities in m/s from the mid plane of the LPA. For the CFD simulations (Left) and MRI (Right). The bottom image represents a visualization of velocity over time calculated from the MRI sets. The velocity is from the inlet and this is only being used as a representation of time.

Figure 4.4 on the following page represents the validation results for subject 18. The CFD results are shown on the left while the MRI results are shown on the right. One validation slice from the middle of the MPA was used at the same time points as the other validation figures. Although the peak velocities with subject 4 varied (0.2810 m/s from CFD to 0.2 m/s from MRI data, qualitatively the peaks are happening in the same location with the peak systolic velocities occurring to the top left of the slice in both the

CFD and MRI. Again, this model was much closer quantitatively than the control subject, only differing by .08 m/s, and qualitatively, peaks and changes in velocity were occurring in the relatively same locations of the model aside from during diastole (C).

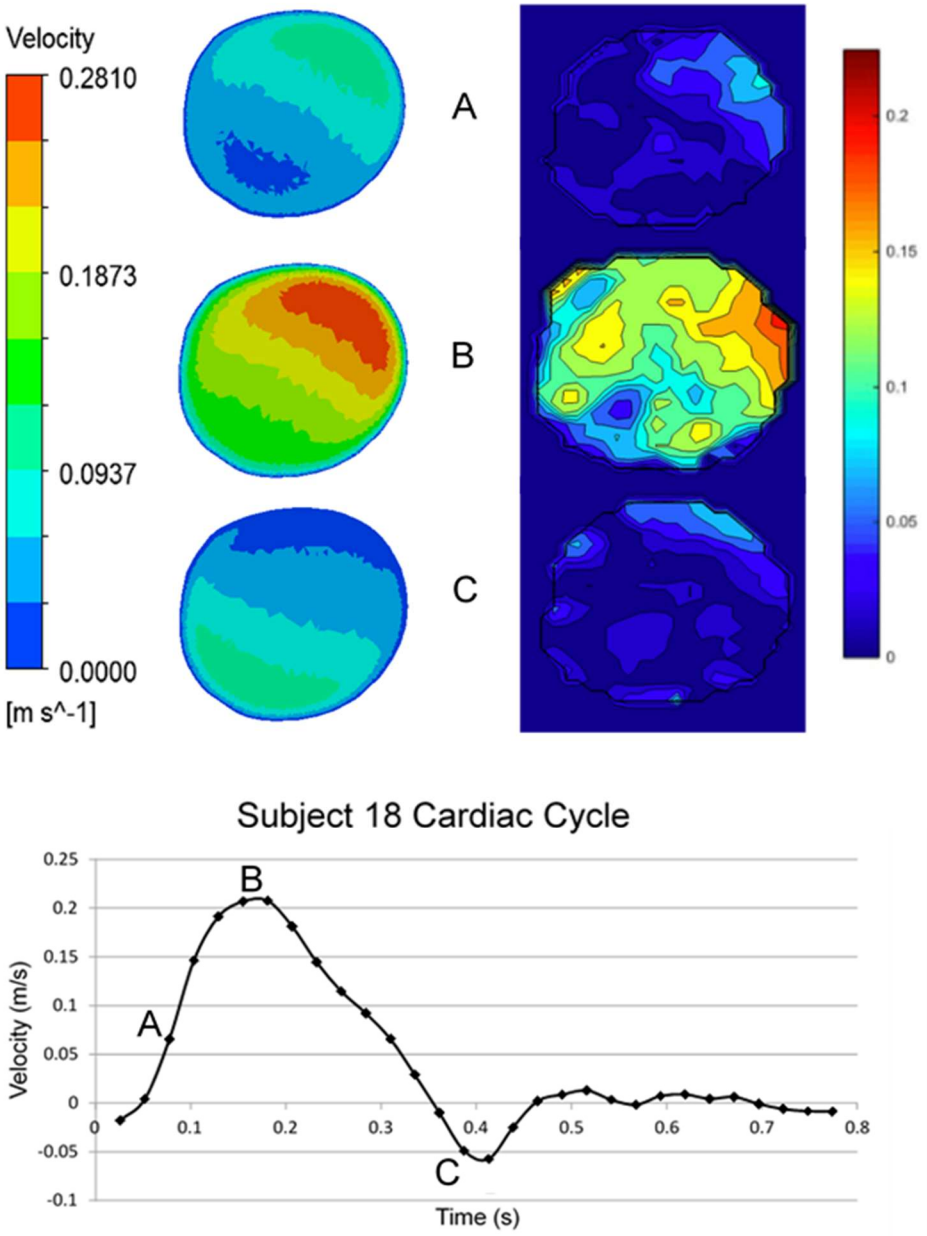

Figure 4.4 Validation of Subject 18 Simulations Using MRI velocities in m/s from the mid plane of the MPA. For the CFD simulations (Left) and MRI (Right). The bottom image represents a visualization of velocity over time calculated from the MRI sets. The velocity is from the inlet and this is only being used as a representation of time.

4.3 Wall Shear Stress Results

This section displays all of the CFD calculated WSS results, including contour plots of the WSS at peak systole for both mesh sizes (finest mesh pre-increasing mesh density near the wall and finest mesh post-increasing mesh density near the wall) (Figures 4.5-4.8) for both the healthy subject (subject 14) and the PAH subjects (subjects 16, 17, and 18). The max WSS pre-increasing the mesh density near the wall occurred in the control subject with an average maximum over the three cardiac cycles of 4.56 dyn/cm^2. This maximum occurred near the outlets after the split into the LPA and RPA at peak systole. The PAH subjects had maximum WSS ranging from 0.63 dyn/cm^2 to 1.02 dyn/cm^2. Minimum WSS for all four subjects were close to zero, with the control subject having a slightly higher average of 0.00126 dyn/cm^2. These minimums occurred during diastole and primarily in the MPA. Table 4.2 on the following page below summarizes minimum (over the entire domain), maximum (over the entire domain) and time and spatially averaged WSS values calculated from CFD for the cases pre-increasing the mesh density near the vessel wall. Multiple cycles were ran to eliminate any potential starting effects of the simulations; however, after running each model through three cardiac cycles the results were found to be consistent through each cycle. Since the WSS, in diastole, was primarily zero throughout the domain, the contours at those points were not included.

Table 4.2 Summary of WSS Data Generated from CFD pre-increasing the mesh density near the wall. Subject 14 is the control and Subjects 16, 17, and 18, are the PAH subjects.

Subject	Cycle	Max WSS (dyn/cm^2)	Min WSS (dyn/cm^2)	Time Averaged WSS (dyn/cm2)
14	*1*	4.555580	0.001256530	0.11167300
	2	4.560470	0.001262460	
	3	4.555490	0.001275720	
	Average	*4.557180*	*0.001264903*	
16	*1*	1.015000	0.000026578	0.01068649
	2	1.015000	0.000090471	
	3	1.015000	0.000115684	
	Average	*1.015000*	*0.000077578*	
17	*1*	0.590426	0.000307290	0.00320149
	2	0.601287	0.000383835	
	3	0.601024	0.000397813	
	Average	0.597579	0.000362979	
18	*1*	0.619380	0.000242789	0.00465446
	2	0.626714	0.000524308	
	3	0.630117	0.000540579	
	Average	0.625404	0.000435892	

The maximum WSS post-increasing the mesh density near the wall occurred in the control subject with an average maximum over the three cardiac cycles of 5.596 dyn/cm^2. This maximum occurred near the outlets after the split into the LPA and RPA at peak systole. The PAH patients had maximum WSS ranging from 1.520 dyn/cm^2 to 3.151 dyn/cm^2. Minimum WSS for all four subjects was close to zero, with the control subject having a slightly higher average of 0.01141 dyn/cm^2. These minimums occurred during diastole and primarily in the MPA. Table 4.3 on the following page summarizes minimum (over the entire domain), maximum (over the entire domain) and time and spatially averaged WSS values calculated from CFD for the cases ran post-increasing the mesh density near the vessel wall. Since at diastole, the WSS was primarily zero throughout the domain, the contours at those points were not included.

Table 4.3 Summary of WSS Data Post Increasing Mesh Density Near the Wall

Subject	Cycle	Max WSS (dyn/cm^2)	Min WSS (dyn/cm^2)	Time Averaged WSS (dyn/cm^2)
14	*1*	5.593	0.0000710	0.01141
	2	5.605	0.0000697	
	3	5.59219	0.0000583	
	Average	*5.59673*	*0.0000663*	
16	*1*	3.15079	0.0000367	0.00109
	2	3.15079	0.0000276	
	3	3.15073	0.0000309	
	Average	*3.15077*	*0.0000317*	
17	*1*	1.5999	0.0000062	0.00032
	2	1.59994	0.0000085	
	3	1.59992	0.0000106	
	Average	*1.59992*	*0.0000084*	
18	*1*	1.52063	0.0000199	0.00046
	2	1.52063	0.0000350	
	3	1.52062	0.0000268	
	Average	*1.52063*	*0.0000272*	

Figure 4.5 on the following page shows both a WSS contour map at peak systole for subject 14 pre and post increasing the mesh density near the wall of the vessel. Subject 14 had a peak WSS of 0.4560 Pa or 4.560 dyn/cm^2 pre-increasing the mesh density near the wall and 5.596 dyn/cm^2 post increasing the mesh density near the wall. With a minimum WSS occurring during diastole when there was a negative velocity profile. The highest areas of WSS occurred on sides opposite of the dilated area of the main pulmonary artery as well as after the immediate split into the left and right pulmonary arteries. Qualitatively the WSS values are very similar with peaks and changes happening in the same location geometrically, with the primary differences being the magnitude of WSS's calculated.

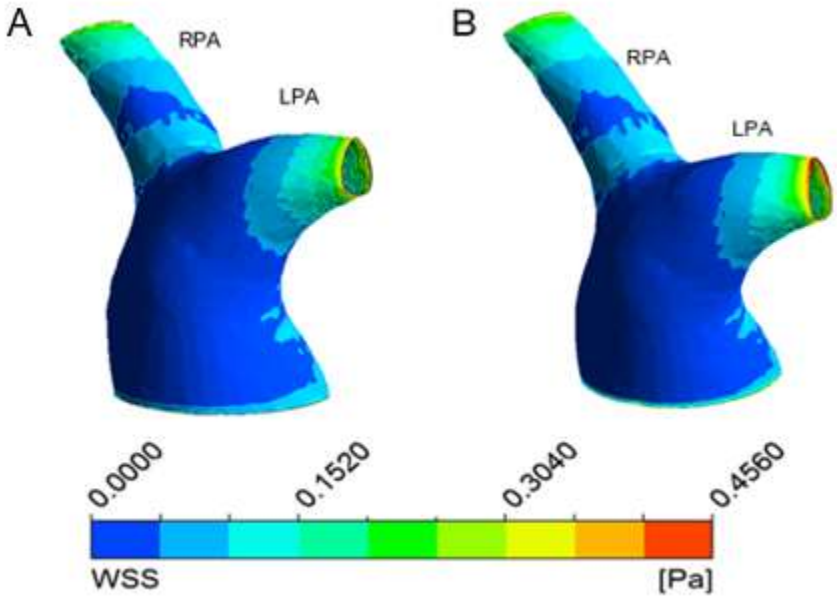

Figure 4.5 WSS Contours for Subject 14 at Peak Systole for the mesh pre-increasing density near the wall (A) and post increasing density near the wall (B).

Figure 4.6 on the following page shows both a WSS contour map at peak systole for subject 16 pre and post increasing the mesh density near the wall of the vessel. Subject 16 had a peak WSS of 0.1015 Pa or 1.015 dyn/cm^2 pre-increasing the mesh density near the wall and 3.151 dyn/cm^2 post increasing the mesh density near the wall. The minimum WSS occurred during diastole when there was a negative velocity profile. The highest areas of WSS occurred on sides opposite of the enlarged mid-section area of the MPA as well as after the immediate split into the left and right pulmonary arteries. Qualitatively the models are very similar with peaks and changes in WSS happening in the same location geometrically, with the primary differences being the magnitude of WSS's calculated. There does appear to be a larger increase in WSS in the RPA compared to the LPA in both models however.

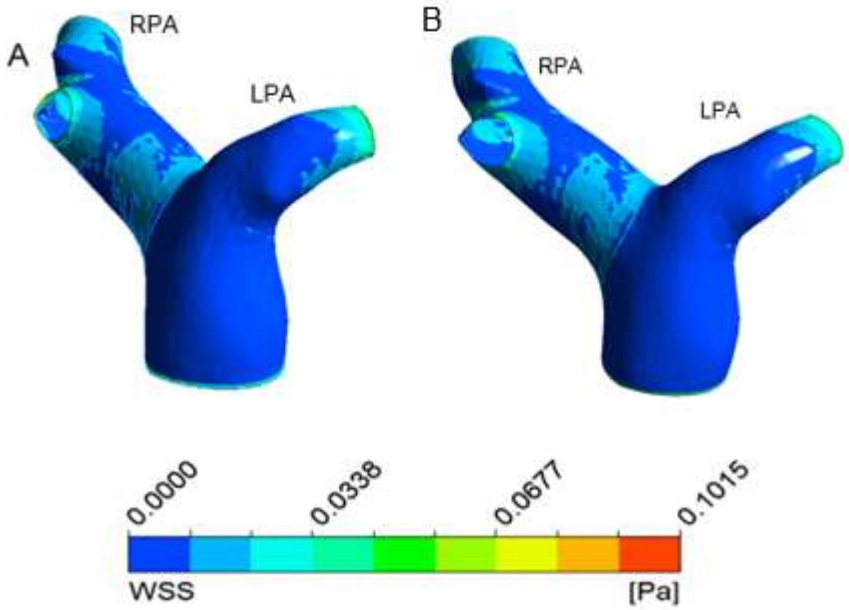

Figure 4.6 WSS Contours for Subject 16 at Peak Systole for the mesh pre-increasing density near the wall (A) and post increasing density near the wall (B)

Figure 4.7 on the following page follows the same formatting as the above figures. Subject 17 had a peak WSS of 0.0597 Pa or 0.5979 dyn/cm^2 pre-increasing the mesh density near the wall and 1.599 dyn/cm^2 post increasing the mesh density near the wall. With a minimum WSS occurring during diastole when there was a negative velocity profile. The highest areas of WSS occurred on sides opposite of the enlarged mid-section of the main pulmonary artery as well as after the immediate split into the left and right pulmonary arteries. Again, the primary difference in WSS is quantitatively in terms of the magnitude of WSS, while qualitatively the models are almost identical. However, compared to subject 16, there seemed to be a more even distribution of WSS changes between both the RPA and LPA.

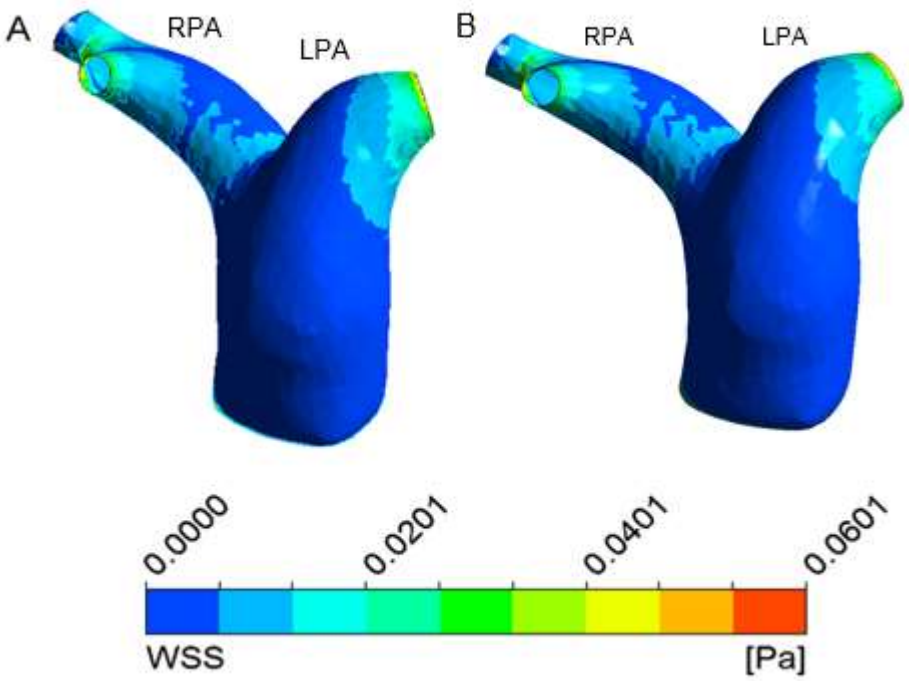

Figure 4.7 WSS Contours for Subject 17 at Peak Systole for the mesh pre-increasing density near the wall (A) and post increasing density near the wall (B)

Figure 4.8 on the following page follows the same formatting used for the rest of the WSS figures. Subject 18 had a peak WSS of 0.0625 Pa or 0.6254 dyn/cm^2 pre-increasing the mesh density near the wall and 1.521 dyn/cm^2 post increasing the mesh density near the wall. With a minimum WSS occurring during diastole when there was a negative velocity profile. The highest areas of WSS occurred on sides opposite of the dilated area of the main pulmonary artery as well as after the immediate split into the left and right pulmonary arteries.

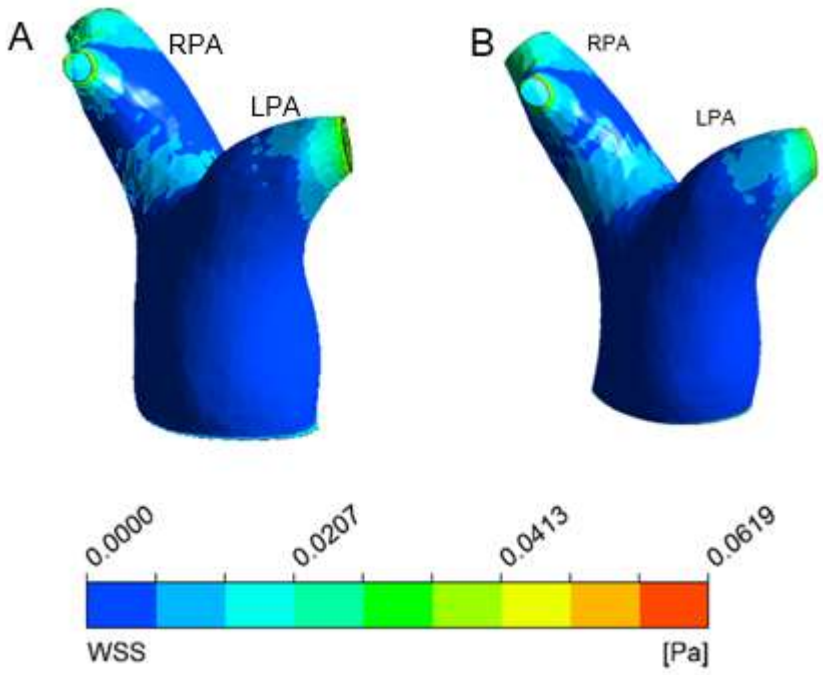

Figure 4.8 WSS Contours for Subject 18 at Peak Systole for the mesh pre-increasing density near the wall (A) and post increasing density near the wall (B)

4.4 Velocity Results

4.4.1 CFD Velocity Results

This section displays all of the CFD calculated velocity results, including volume rendered plots of the velocity at both peak systole and diastole (Figures 4.13-4.16), as well as velocity contours at both the left and right pulmonary artery outlets over 4 time points of each subjects' cardiac cycle (Figures 4.18-4.21). These plots were developed from the finest created mesh, pre-increasing the mesh density near the vessel wall. Because the flow through the models doesn't align directly with one axis, velocity magnitude was used. The control subject had the highest maximum velocity with an average of 3.572 m/s while the remaining subjects had average maximum velocities ranging from 0.803 m/s to 1.071 m/s. Table 4.4 on the following page summarizes

minimum, maximum and time averaged velocity values for each subject over multiple cardiac cycles. Overall, there was a reduction in both maximum and time averaged velocities between the control (subject 14) and the PAH subjects (16, 17, and 18). Again, similar to the WSS there was little discrepancies between the cycles.

Table 4.4 Summary of Velocity Data Generated From CFD

Subject	Cycle	Maximum Velocity (m/s)	Time Averaged (m/s)
14	*1*	3.571	0.24289
	2	3.573	
	3	3.571	
	Average	3.572	
16	*1*	1.072	0.05837
	2	1.070	
	3	1.071	
	Average	1.071	
17	*1*	0.841	0.02171
	2	0.834	
	3	0.835	
	Average	0.837	
18	*1*	0.807	0.02250
	2	0.802	
	3	0.800	
	Average	0.803	

Figure 4.9 on the following page shows volume rendered velocity contours for subject 14 at both peak systole and diastole. The maximum velocity magnitude for subject 14 was 3.5730 m/s, occurring at the outlets, this is significantly higher than expected. There were increases in the velocity after the immediate branching into the left and right PA.

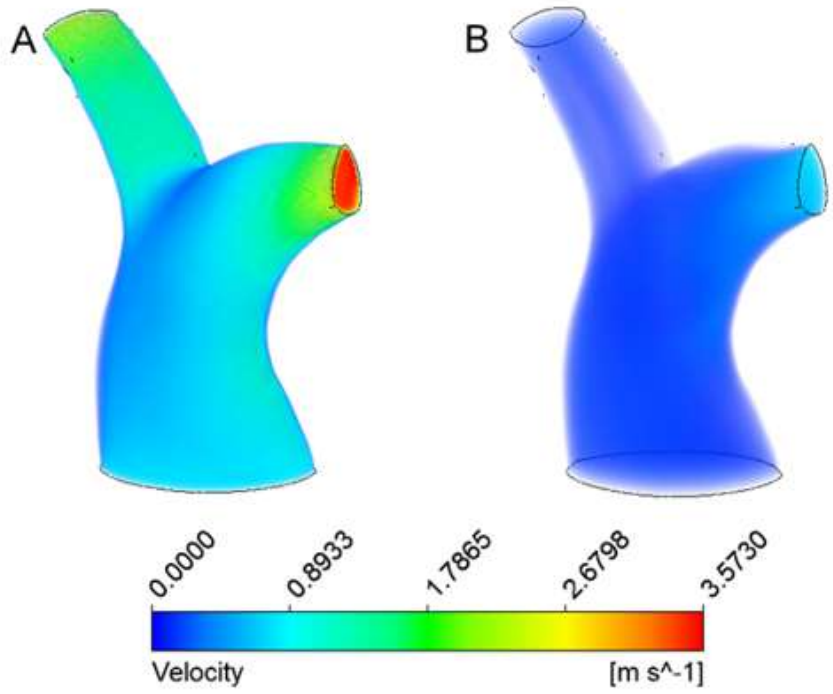

Figure 4.9 Volume Rendered Velocity Plots of Subject 14 at both Peak Systole and Diastole (A and B)

Figure 4.10 on the following page shows the volume rendered velocity contour for subject 16. Again, the maximum velocity for subject 16 was roughly 1.07 m/s occurring near the outlets of the model, with reduced flow within the dilated areas as well as increases in flow after breaks in the artery.

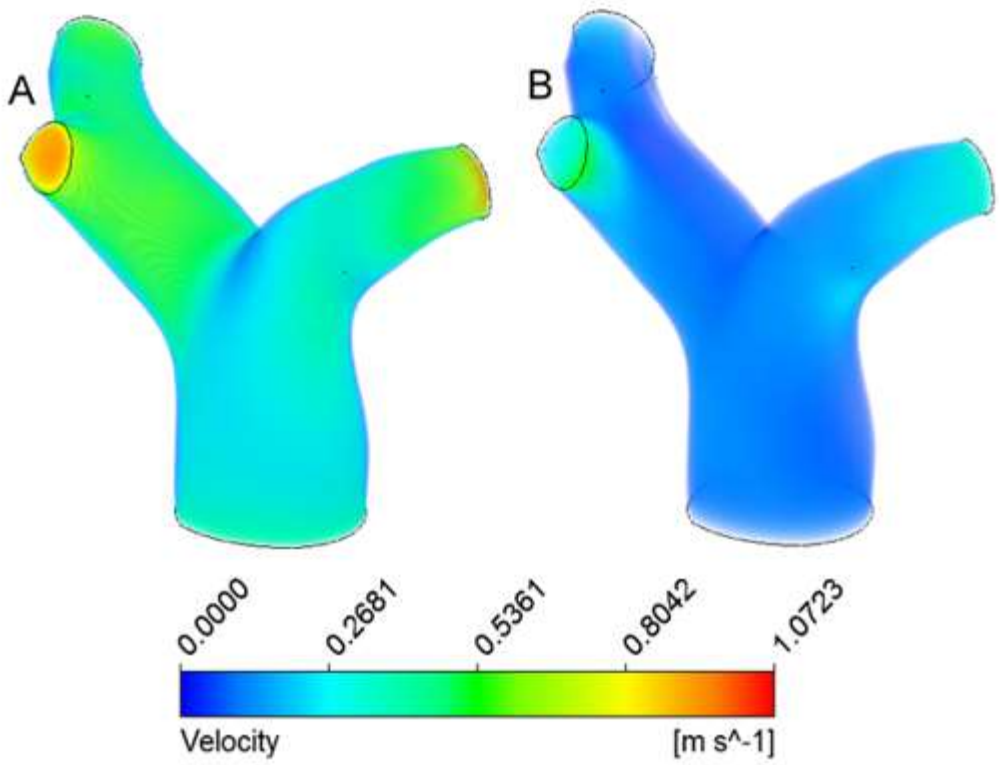

Figure 4.10 Volume Rendered Velocity Plots of Subject 16 at both Peak Systole and Diastole (A and B)

Figure 4.11 on the following page shows the volume rendered velocity plot of subject 17. This shows similar trends to subject 16, with reduced areas of velocity in the dilated section of the main pulmonary artery (shown as dark blue), as well as the maximum velocities occurring near the outlets (0.8408 m/s) with increase overall after flow splits.

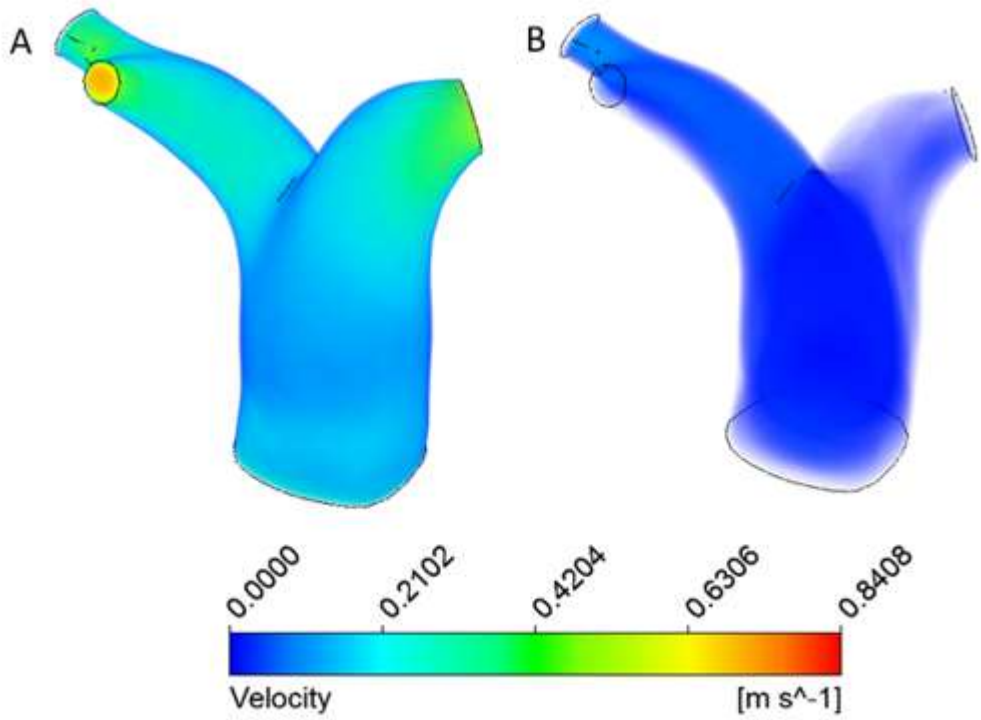

Figure 4.11 Volume Rendered Velocity Plots of Subject 17 at both Peak Systole and Diastole (A and B)

Subject 18 in Figure 4.12 on the following page followed the trends of the rest of the PH subjects. The maximum velocities occurred towards the outlets (0.8076 m/s) with increases in velocities after splits in the PA as well as reduced flow near the dilated MPA.

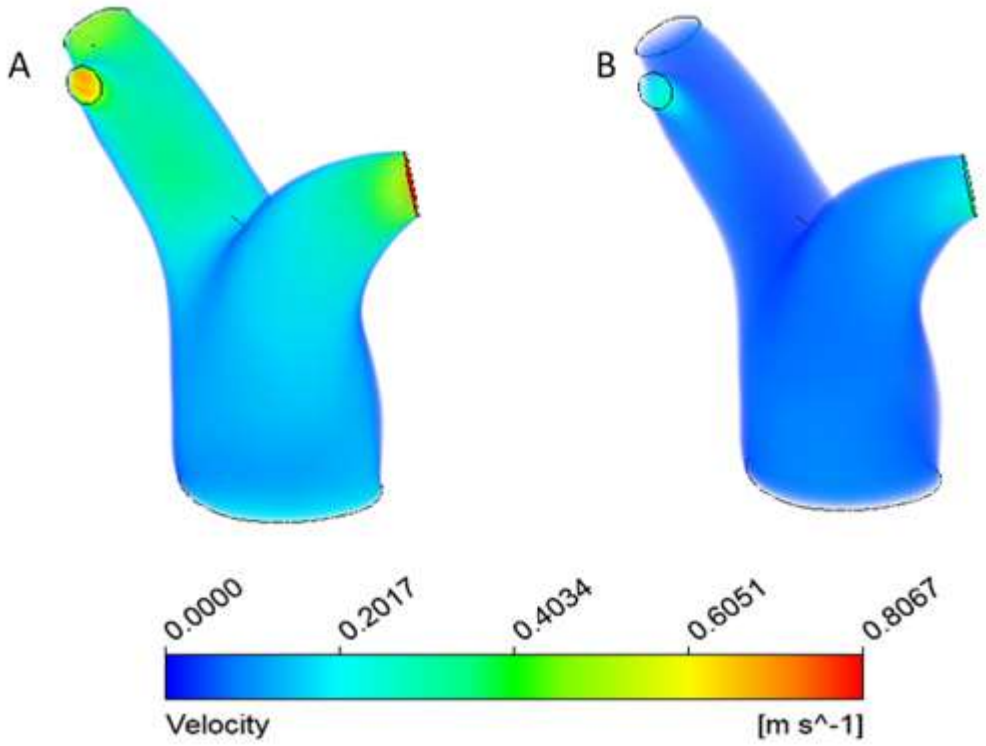

Figure 4.12 Volume Rendered Velocity Plots of Subject 18 at both Peak Systole and Diastole (A and B)

Figure 4.13 on the following page is the volume rendered velocity plot for subject 18, after increasing the mesh density near the wall of the PA. There was very little change in the velocity both qualitatively and quantitatively, with maximums and lows occurring near the same spots of the geometry as well as the maximum velocity only changing from 0.8067 m/s to 0.7825 m/s. Based on this information, the remaining volume rendered plots are not included as there was no worthwhile comparisons to be made between the two simulation types.

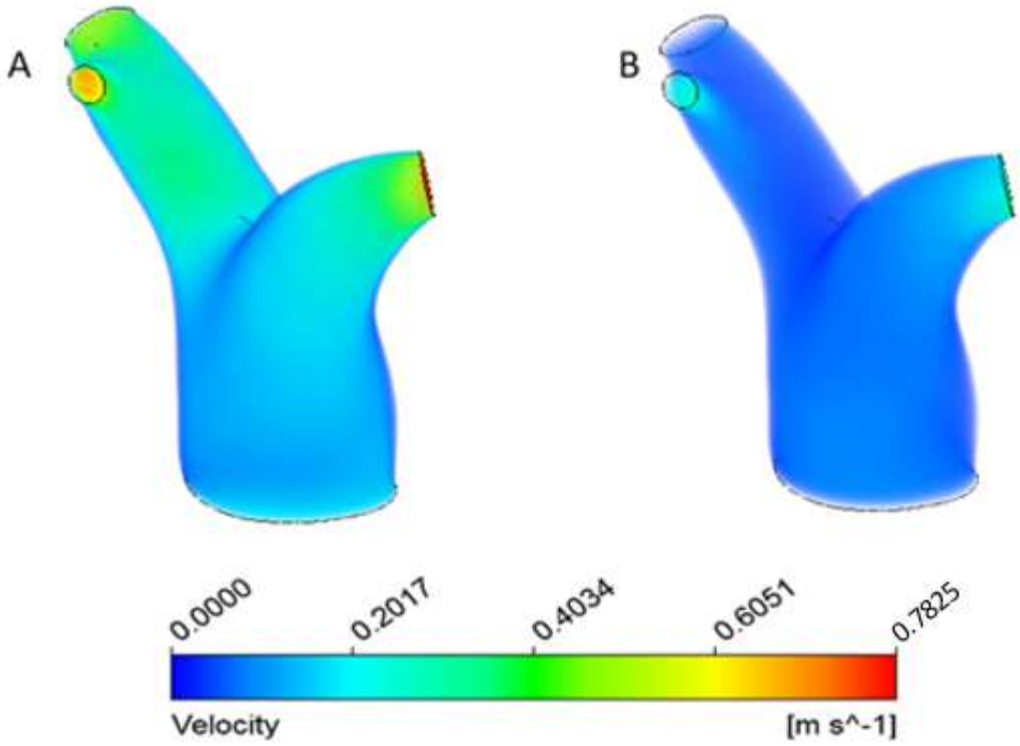

Figure 4.13 Volume Rendered Velocity Plots of Subject 18 at both Peak Systole and Diastole (A and B) (Post Mesh Density Increase near the Wall).

Figure 4.14 on the following page is a velocity contour plot of subject 14, plotting the outlet velocities of both the LPA and RPA outlets (left and right respectively). The bottom figure is a time representation, taken from the MRI data prescribed to the inlet. Four time points were used, half way to peak systole, peak systole, half way to diastole, and diastole (A, B, C, and D respectively). Peak velocities occurred during peak systole with a maximum of 3.58 m/s and a minimum velocity at diastole of approximately 0 m/s. Qualitatively the flow seems to be consistent throughout the outlets for subject 14;

meaning peaks of flow were happening in the same relative location along the cross section at both outlets.

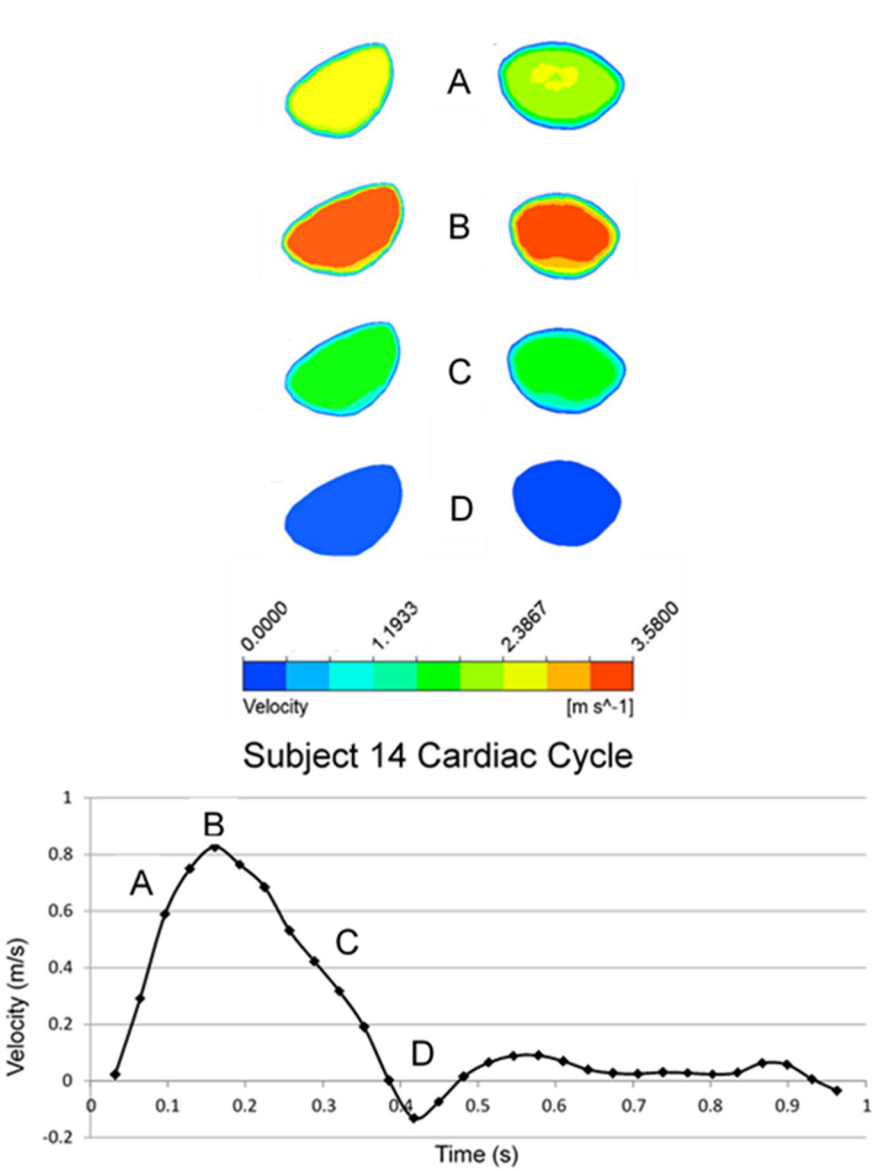

Figure 4.14 Left and Right Pulmonary Artery Velocities Varying throughout a cardiac cycle LPA (Left A-D) and RPA (Right A-D) for subject 14

Figure 4.15 on the following page is formatted the same as the above figures. Peak velocities occurred during peak systole with a maximum of 1.072 m/s and a minimum velocity at diastole of approximately 0 m/s. Qualitatively the flow seems to be

consistent throughout the outlets for subject 16; aside from during peak systole (B) potentially due to the added split in the RPA compared to the LPA. Meaning peak velocities were in the relatively same locations in both outlets as well as any changes in velocity occurring in the same relative pattern and location.

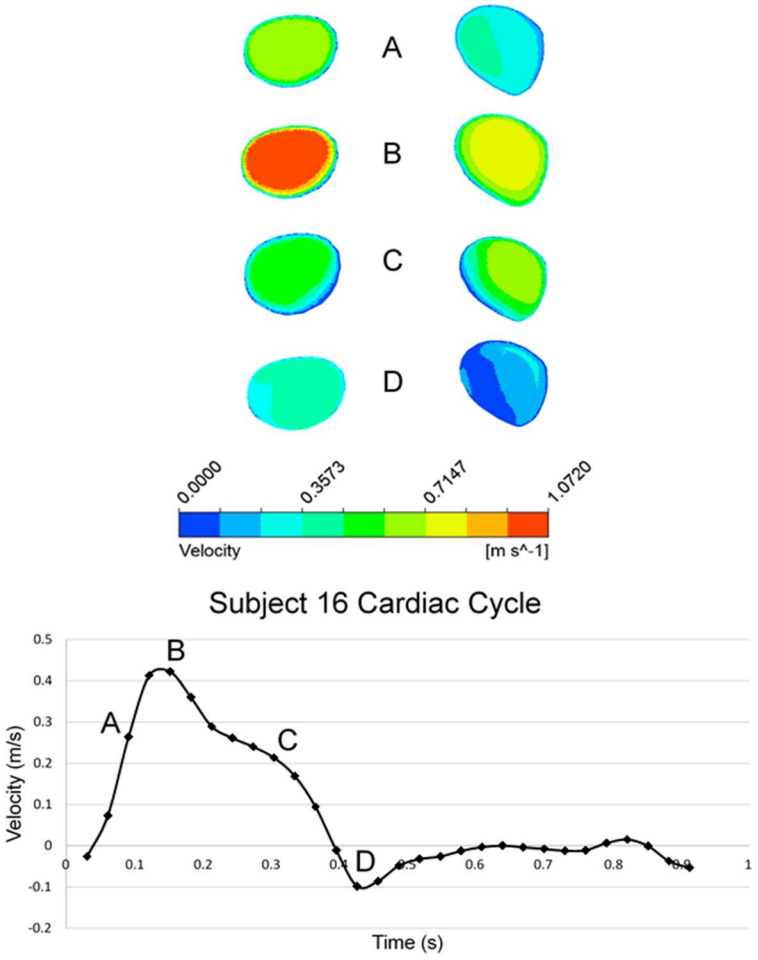

Figure 4.15 Left and Right Pulmonary Artery Velocities Varying throughout a cardiac cycle LPA (Left A-D) and RPA (Right A-D) for subject 16

Figure 4.16 on the following page is formatted the same as the other figures in this section. Peak velocities occurred during peak systole with a maximum of 0.8451 m/s and a minimum velocity at diastole of approximately 0 m/s. Qualitatively the flow seems

to be consistent throughout the outlets for subject 17; aside from during peak systole (B) potentially due to the added split in the RPA compared to the LPA.

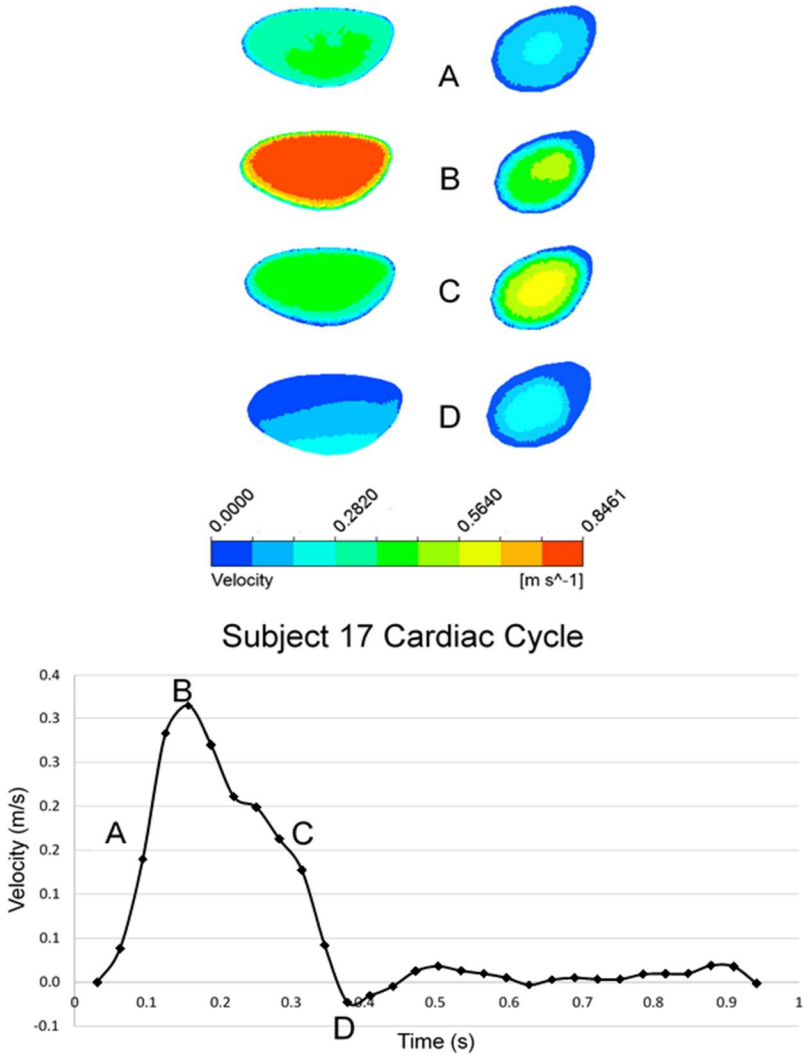

Figure 4.16 Left and Right Pulmonary Artery Velocities Varying throughout a cardiac cycle LPA (Left A-D) and RPA (Right A-D) for subject 17

Figure 4.17 on the following page is formatted the same as the above figures. Peak velocities occurred during peak systole with a maximum of 0.8451 m/s and a minimum velocity at diastole of approximately 0 m/s. Qualitatively the flow seems to be

consistent throughout the outlets for subject 18; aside from during peak systole (B) potentially due to the added split in the RPA compared to the LPA.

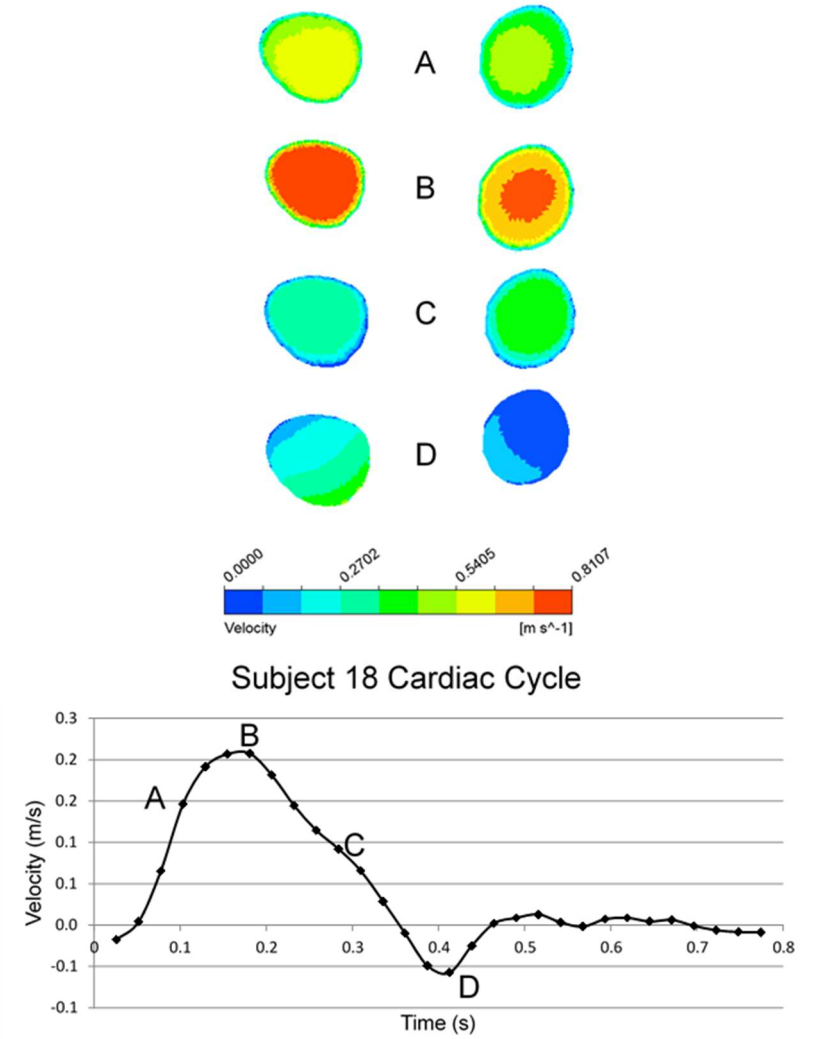

Figure 4.17 Left and Right Pulmonary Artery Velocities Varying throughout a cardiac cycle LPA (Left A-D) and RPA (Right A-D) for subject 18.

CHAPTER 5
DISCUSSION

The overall objective of this thesis was to, using MRI and CFD, quantify changes in wall shear stress throughout the pulmonary artery when compared to a normotensive control subject. With the future goal of this knowledge potentially being used to be able to diagnose PH non-invasively using changes in WSS.

In order to have a validation method of sorts, the velocity contours returned from the MATLAB program were compared at various time points throughout each subjects' second simulated cardiac cycle, these can be seen in Figures 4.1-4.4. These data were collected at points other than at a boundary condition. For subjects 16 and 18, new velocity data was calculated at the middle of the MPA, while the middle of the LPA was used for subjects 14 and 17, since there were no middle MPA image sets available to use. The goal was to compare, qualitatively, the similarities between the CFD results and the MRI results. It should be noted that a slight modification to the original MATLAB code was introduced in order for it to plot velocity magnitude, as well as change the scales to be as close as possible to the CFD scales. Overall, all four subjects' validation models correlate qualitatively. Peak areas of velocity occur on the same side of the models, with similar flow patterns throughout the arterial cross-section. Quantitatively, however, with subjects 16 and 18, the peak velocities were within hundredths of m/s while subject 17 was within tenths and subject 14 was approximately one m/s different. The differences could potentially be explained by, differences in

geometrical location, compared to boundary conditions; the slices obtained for 14 and 17 were obtained further away from the inlet, potentially allowing for more changes to occur in flow patterns.

Again, the most significant differences in the validation models were with subject 14, where the CFD showed a maximum velocity of 1.83 m/s compared to the maximum of roughly 0.6 m/s calculated using the MRIs. Although care was taken to attempt to pick the location closest to that of the MRI slice, segmentation and smoothing errors could have caused these discrepancies in size. Another potential source of error that could have led to this discrepancy would be the lack of a flow split in subject 14 near the outlets, compared to the PH subjects; the lack of this split could have caused extra flow to go through the right LPA in the model instead of being diverted to the extra split in the RPA.

The WSS contour maps (Figures 4.5-4.8, Pgs. 47-50) of subjects 14, 16, 17, and 18 at peak systole both pre-increasing the mesh density near the wall and post increasing the mesh density near the wall are quantitatively different. When comparing the maximum systolic WSS between the two mesh densities used, the control's maximum increased from 4.56 dyn/cm^2 to 5.597 dyn/cm^2; while the PAH subjects increased the range of their WSS from 0.63 dyn/cm^2 - 1.02 dyn/cm^2 to 1.521 - 3.1511 dyn/cm^2. This was due to the greater resolution of the velocity gradient near the wall. Figure 4.13 (Pg. 57) shows, a volume rendered velocity profile for subject 18 post increasing mesh density

near the wall; this image was used as a way to show that increasing the mesh density had little to no effect on the velocity values calculated through CFD.

Tang et. al. showed a time average of approximately 20.5 ± 4.0 dynes/cm^2 in the proximal pulmonary arteries of healthy subjects (averaged over 10 mm strips). The average for this study was 0.112 dyn/cm^2, however, this was averaged over the entirety of the model including the majority of the model being comprised of areas with little to no WSS. In addition, this study only included one control subject (who also had sickle cell disease) while Tang is an average of 5 control and 5 PAH subjects. Another discrepancy between the results is the smaller overall model size; subject 14's model diameter was roughly 2.36 cm with an average MRI calculated flow rate of 4.77 L/min, while the diameter of the control subjects in the Tang et al. paper ranged from 2.6-2.8 cm with flow rates ranging from 5.1-6.6 L/min. All of these factors along with the fact that subject 14 is not a "true" control as they also have sickle cell disease could account for these differences. One last possible cause is the difference in solvers used, Tang et. al. used a finite element solver with a parabolic profile versus the current study which used Fluent, a finite volume solver with a blunt velocity profile.

However, using the modified Poiseuille equation discussed earlier, the WSS values were calculated from the MRI results. The maximum MRI WSS values (at peak systole) were 5.40, 2.84, 1.35, and 1.18 dynes/cm^2 for subjects 14-18 respectively. The CFD simulated maximums during peak systole were 5.59, 3.15, 1.59, and 1.52 dynes/cm^2 for subjects 14-18 respectively. These values are much closer and again, the differences

can be explained by the differences in the relative geometry size, between the MRI segmentation and CFD segmentation.

Barker et. al. using 4DMRI found a WSS at peak systole of 1.9 ± 0.7 dyn/cm^2 for the PH population and 5.4 ± 2.1 dyn/cm^2 for Barker's healthy population; both of these averages were taken in the RPA. The RPA values were used as comparison because that is where the maximums primarily occurred in the current studies subjects. These values are spatially averaged over a cross-section of the pulmonary artery at peak systole. If the exact location could be used for comparison it would be beneficial to compare a spatially averaged cross-sectional WSS value from the current study to barkers.

Overall, the results correlate to the expected trend, that an increase in pulmonary vasculature resistance, 0.87-13.9 Wood units in PH subjects**,** would decrease the WSS. The maximum WSS decreased from 1.02 dynes/cm^2 at 0.87 wood units to 0.62 0.62 dynes/cm^2 at 13.9 wood units. It should also be noted, that similar to the previously discussed studies (Kheyfets, 2015 and Tang, 2012), areas of increased WSS in the PH models were on sides opposite the enlarged midsection of the MPA.

Figures 4.9-4.12 (Pg. 52-55) show volume rendered velocity profiles for subjects 14, 16, 17, and 18 respectively at both peak systole and diastole pre increasing mesh density near the wall. Decreased velocities can be seen in the enlarged MPAs, while increased velocities can be seen following branching, in areas opposite of increases in arterial

diameter. Peak velocities were found near branching and near the outlets, where the arterial diameters were smaller. Again, similar to the WSS data, the maximum velocity of subject 14, was roughly 4 times greater than that of the PH subjects.

Figures 4.14-4.17 (Pg. 57-60) show velocity contours at the outlets. Similar to the volume rendered velocity plots, the control subjects' outlet velocity was approximately 4 times greater than the PH subjects. There was a clear decrease in velocity of the RPA within the PH subjects compared to the control subject. This can be explained by the flow split close to the outlets of the PH subjects that wasn't able to be imaged in the control subjects MRIs.

The most significant differences in the outlet velocity models were with subject 14, where the CFD showed a maximum velocity of 3.58 m/s compared to the maximum of 0.5589 m/s calculated using the MRIs and MATLAB. While this is a significant difference, the area of the inlet determined from MRI was an average of 5.7 cm^2 while the area of the recreated models inlet was 4.36 cm^2. This could be a result of possible segmentation errors, as well as post processing of the model (i.e. cutting the outlets perpendicular to the flow direction) as well as smoothing errors. After fitting the MR flow rate to the area of the model inlet, the maximum inlet velocity was 0.8264 m/s. This value differs from the MR maximum velocity (0.5589 m/s), however the flow rate is the same. If a more automated source of segmentation could be created, this would eliminate the human error in manual corrections and provide even more identical 3D

models that would no longer limit the simulations results. In future work, it would be more beneficial to compare flow rates at the outlets rather than velocities.

Although the data gathered were typically lower than other published studies; overall, the trends of a decrease in WSS in a PH population as well as decreases in velocity were still seen. The primary limitations of this study were the population size, as well as the inability to model further out into the pulmonary vasculature as many other studies have been capable of doing. This is primarily due to the use of MRI over CT scanning. Although precautions were taken to limit errors in segmenting and 3D regeneration (i.e. having the segmentation looked over by a cardiologist), this process contained a significant portion of manual corrections that could potentially be a significant source of error. These same manual sources of error also apply towards the MRI data processing. In the future, it may be beneficial to calculate a systolic WSS instead of an average over the whole cardiac cycle. Doing so may elucidate greater differences between controls and PH patients.

To further this study, it would be beneficial to perform a method of analyses similar to Tang et. al., where WSS was average over a 10-mm band on both the LPA and RPA rather than over the entire geometry. However, in order to do this, separate post processing scripts would need to be written to create the 10 mm strips perpendicular to the vessel wall. If possible either, modeling further out with MRI or using CT to model the geometry while using MRI for flow parameters could increase the accuracy of the simulations by potentially increasing the accuracy of the model recreation. Although,

Kheyfets et. al. performed a study essentially eliminating the need for a complex boundary condition at any outlets, attempting to prescribe patient specific pressure conditions to the outlets would also potentially increase the accuracy of the results.

CHAPTER 6
CONCLUSION

Pulmonary hypertension (PH), as defined by a mean pulmonary arterial pressure (mPAP) greater than 25 mmHg, is a life-threatening chronic disorder of the pulmonary circulation which leads to right ventricle failure and if untreated, death. The purpose of this work was to use both, MRI and CFD, to quantify changes in wall shear stress throughout the pulmonary artery of a PH population when compared to a normotensive control subject. With the future goal of this knowledge potentially being used to be able to diagnose PH non-invasively using changes in WSS. Patient's PA's were recreated using MRIs and MIMICS software. Velocity profiles were generated from the MRIs using MATLAB and CFD simulations were conducted using Fluent 17.0. The control subject showed a 1.5 to 3.5 times increase in maximum WSS compared to the PH subjects. Although the overall WSS values of these tests are approximately 5 times lower than those of the previously discussed studies (Tang 2012), the trends found in this study quantitatively (relatively) and qualitatively match with Tang's results. The results also correlate well with MRI calculated WSS from both this study and Barker et. al. Future work still needs to be done with both a larger population size, potentially modeling further into the pulmonary vasculature as well as attempting different methods of data post-processing.

REFERENCES

Badesch D. B., Champion H. C., Gomez S. M., et al. Diagnosis and Assessment of Pulmonary Arterial Hypertension. J Am Coll Cardiol. 2009; 54(1s1):S55-S66.

Barbara Woodward Lips Patient Education Center. Pulmonary hypertension. Rochester, Minn.: Mayo Foundation for Medical Education and Research; 2015

Barker, A. J., Roldán-Alzate, A., Entezari, P., Shah, S. J., Chesler, N. C., Wieben, O., François, C. J. 4D Flow Assessment of Pulmonary Artery Flow and Wall Shear Stress in Adult Pulmonary Arterial Hypertension: Results from Two Institutions. Magnetic Resonance in Medicine : Official Journal of the Society of Magnetic Resonance in Medicine / Society of Magnetic Resonance in Medicine. 2015; 73(5), 1904–1913.

Botney, M. D. Role of hemodynamics in pulmonary vascular remodeling: implications for primary pulmonary hypertension. Am. J. Respir. Crit. Care Med. 1999; 159:361–364,

Boundless. “Systemic and Pulmonary Circulation.” Boundless Anatomy and Physiology. Boundless, 08 Aug. 2016. Retrieved 21 Sep. 2016

Boutsianis E., Gupta S., Boomsma K., and Poulikakos D. “Boundary Conditions by Schwarz-Christoffel Mapping in Anatomically Accurate Hemodynamics,” Ann. Biomed. Eng. 2008; 36(12), pp. 2068–2084

Bove E. L., De Leval M. R., Migliavacca F., Guadagni G., and Dubini G. “Computational Fluid Dynamics in the Evaluation of Hemodynamic Performance of Cavopulmonary Connections After the Norwood Procedure for Hypoplastic Left Heart Syndrome,” J. Thorac. Cardiovasc. Surg. 2003; 126(4), pp. 1040–1047

Boxt L. M., Katz J. “Magnetic resonance Imaging for Quantitation of Right Ventricular Volume in Patients with Pulmonary Hypertension,” Journal of Thoracic Imaging. 1993; 8:92-97

Burrowes K. S., Hunter P. J., and Tawhai M. H. “Anatomically Based Finite Element Models of the Human Pulmonary Arterial and Venous Trees Including Supernumerary Vessels,” J. Appl. Physiol. 2005; 99(2), pp. 731–738

Christophe J. J., Ishikawa T., Imai Y., Takase K., Thiriet M., and Yamaguchi T. “Hemodynamics in the Pulmonary Artery of a Patient with Pneumothorax,” Med. Eng. Phys. 2012; 34(6), pp. 725–732

Ebrahimdoost Y., Qanadli S. D., Nikravanshalmani A., Ellis T. J., Shojaee Z. F., and Dehmeshki J. “Automatic Segmentation of Pulmonary Artery (PA) in 3D Pulmonary CTA Images,” 17th International Conference on Digital Signal Processing (DSP). 2011; pp. 1–5

Formaggia L., Lamponi D., and Quarteroni A., 2003, “One-Dimensional Models for Blood Flow in Arteries,” J. Eng. Math., 47(3), pp. 251–276

Galiè, N., Corris, P. A., Frost, A., Girgis, R. E., Granton, J., Jing, Z. C., Keogh, A. Updated treatment algorithm of pulmonary arterial hypertension. European Heart Journal. 2009; 30, 2493-2537

George S. M., Eckert L. M., Martin D. R., and Giddens D. P. Hemodynamics in Normal and Diseased Livers: Application of Image-Based Computational Models. Cardiovascular Engineering and Technology. 2014; pp. 1-12

George S. M., Ghasemi P., Mehra S., Sharma S., and Cahill J. Investigation of Pulmonary Artery Hypertension in Patients with Sickle Cell Disease. 2012 Biomedical Engineering Society Annual Meeting. Atlanta, Georgia. October 2012.

Giaid A, Saleh D. Reduced expression of endothelial nitric oxide synthase in the lungs of patients with pulmonary hypertension. N Engl J Med. 1995; 333:214–21.

Giaid A, Yanagisawa M, Langleben D, Michel RP, Levy R, Shennib H, et al. Expression of endothelin-1 in the lungs of patients with pulmonary hypertension. N Engl J Med. 1993; 328:1732–9.

Hebson, C., New, T., Record, E., Oster, M., Ehrlich, A., Border, W. Kanaan, U. Elevated tricuspid regurgitant velocity as a marker for pulmonary hypertension in children with sickle cell disease: Less prevalent and predictive than previously thought? Journal of Pediatric hematology/oncology. 2014; 37(2), 134-139.

Hunter K. S., Lanning C. J., Chen S. Y., Zhang Y., Garg R., Ivy D. D., and Shandas R., “Simulations of Congenital Septal Defect Closure and Reactivity Testing in Patient-Specific Models of the Pediatric Pulmonary Vasculature: A 3D Numerical Study with Fluid-Structure Interaction,” ASME, J. Biomech. Eng. 2006; 128(4), pp. 564–572

Hunter K. S., Lee P. F., Lanning C. J., Ivy D. D., Kirby K. S., Claussen L. R., Chan K. C., and Shandas R., “Pulmonary Vascular Input Impedance Is a Combined Measure of Pulmonary Vascular Resistance and Stiffness and Predicts Clinical Outcomes Better Than Pulmonary Vascular Resistance Alone in Pediatric Patients with Pulmonary Hypertension,” Am. Heart J. 2008; 155(1), pp. 166–174

Hunter K. S., Feinstein J. A., Ivy D. D., and Shandas R., 2010, “Computational Simulation of the Pulmonary Arteries and Its Role in the Study of Pediatric Pulmonary Hypertension,” Prog. Pediatr. Cardiol, 30(1–2), pp. 63–69

Humbert M, Olivier S., Ari C., Michèle B., Gilbert H., Virginie G., Azzedine Y., Emmanuel W., Jean-François C., François C., Claire D., Christophe P., Martine R., Alain H., Marcel L., Eric H., and Gérald S. "Pulmonary Arterial Hypertension in France", American Journal of Respiratory and Critical Care Medicine, Vol. 173, No. 9 (2006), pp. 1023-1030.

Hyduk A., Croft J.B., Ayala C., et al. Pulmonary Hypertension Surveillance—United States, 1980–2002. MMWR 2005;54(SS05);1–28.

Iffrig, E. M., Taylor, W. R., Oshinski, J. N. A Method for Rapid, Accurate Calculation of Wall Shear Stress from 2D Phase Contrast MRI Data. Bioengineering, and Biotransport Conference (SB3C), Snow Valley, UT. 2015.

Kauczor H. U., Ley-Zaporozhan J., and Ley S. “Imaging of Pulmonary Pathologies: Focus on Magnetic Resonance Imaging,” Proc. Am. Thorac. Soc. 2009; 6(5), pp. 458–463

Kheyfets, V. O., O’Dell, W., Smith, T., Reilly, J. J., & Finol, E. A. Considerations for Numerical Modeling of the Pulmonary Circulation—A Review with a Focus on Pulmonary Hypertension. Journal of Biomechanical Engineering. 2013; 135(6), 0610111–06101115.

Kheyfets VO, Rios L, Smith T, et al. Patient-Specific Computational Modeling of Blood Flow in the Pulmonary Arterial Circulation. Computer methods and programs in biomedicine. 2015; 120(2):88-101

Kulik, T. J. Pulmonary hypertension caused by pulmonary venous hypertension. Pulmonary Circulation. 2014; 4(4), 581-595. Doi: 10.1086/678471

Kung E., and Taylor C., 2011, "Development of a Physical Windkessel Module to Re-Create In Vivo Vascular Flow Impedance for In Vitro Experiments," Cardiovasc. Eng. Tech., 2(1), pp. 2–14

Laffon, E., Francois L., Virginie B., Laurent de B., Dominique D., and Roger M. "Noninvasive assessment of pulmonary arterial hypertension by MR phase-mapping method." J Appl Physiol. 2001; 90: 2197–2202

Lotz J, Meier C, Leppert A, Galanski M. Cardiovascular flow measurement with phase-contrast MR imaging: basic facts and implementation. RadioGraphics. 2002; 22:651-671

McLaughlin VV. McGoon MD. Pulmonary arterial hypertension. Circulation. 2006; 114(13):1417-31

Olufsen M. S., "A One-Dimensional Fluid Dynamic Model of the Systemic Arteries," Stud. Health Technol. Info. 2000; 71, pp. 79–98

Potters, Wouter V., Marquering, Henk A., VanBavel, Ed, Nederveen, Aart J. Measuring Wall Shear Stress Using Velocity-Encoded MRI. Curr Cardiovasc Imaging Rep. 2014; 7:9257

Prakash S., and Ethier C. R. "Requirements for Mesh Resolution in 3D Computational Hemodynamics," ASME J. Biomech. Eng. 2001; 123(2), pp. 134–144

Shah, S. J. Pulmonary hypertension. Jama. 2012; 308(13), 1366-1374.

Sharma, Sunil, et al. "Pulmonary Artery Occlusion Pressure May Over diagnose Pulmonary Artery Hypertension in Sickle Cell Disease." Clinical cardiology. 2013

Simonneau G, Galiè N, Rubin LJ, Langleben D. Seeger W. Domenighetti G. Gibbs S. Lebrec D. Speich R. Beghetti M. Rich S. Fishman A. Clinical classification of pulmonary hypertension. J Am Coll Cardiol. 2004; 43(12, suppl S):5S-12S.

Simonneau G. Robbins IM. Beghetti M. Channick RN. Delcroix M. Denton CP. Elliott CG. Gaine SP. Gladwin MT. Jing ZC. Krowka MJ. Langleben D. Nakanishi N.

Souza R. Updated clinical classification of pulmonary hypertension. Journal of the American College of Cardiology. 2009; 54(1 Suppl): S43-54

Simonneau G, Gatzoulis MA, Adatia I, Celermajer D, Denton C, Ghofrani A, Gomez Sanchez MA, Kumar RK, Landzberg M, Machado RF, Olschewski H, Robbins IM, Souza R. Updated clinical classification of pulmonary hypertension. J Am Coll Cardiol. 2013; 62: D34–41.

Spiegel M. “Patient-Specific Cerebral Vessel Segmentation with Application in Hemodynamic Simulation,” Ph.D. Thesis, Universität Erlangen Nürnberg, Erlangen, Germany. 2011.

Spilker R. L., Feinstein J. A., Parker D. W., Reddy V. M., and Taylor C. A., “Morphometry-Based Impedance Boundary Conditions for Patient-Specific Modeling of Blood Flow in Pulmonary Arteries,” Ann. Biomed. Eng. 2007; 35(4), pp. 546–559

Tang B. T., Fonte T. A., Chan F. P., Tsao P. S., Feinstein J. A., and Taylor C. A. “Three-Dimensional Hemodynamics in the Human Pulmonary Arteries Under Resting and Exercise Conditions,” Ann. Biomed. Eng. 2011; 39(1), pp. 347–358

Beverly T. Tang, Sarah S. Pickard, Frandics P. Chan, Philip S. Tsao, Charles A. Taylor, andJeffrey A. Feinstein, "Wall shear stress is decreased in the pulmonary arteries of patients with pulmonary arterial hypertension: An image-based, computational fluid dynamics study," Pulmonary Circulation 2. 2012; no. 4, 470-476.

Tu J., Yeoh G. H., and Liu C., 2008, Computational Fluid Dynamics—a Practical Approach, Elsevier Inc., Burlington, MA

Vignon-Clementel I. E., Marsden A. L., and Feinstein J. A. “A Primer on Computational Simulation in Congenital Heart Disease for the Clinician,” Prog. Ped. Cardiol. 2010; 30(1–2), pp. 3–13.

Vignon-Clementel I. E., Figueroa C. A., Jansen K. E., and Taylor C. A. “Outflow Boundary Conditions for Three-Dimensional Finite Element Modeling of Blood Flow and Pressure in Arteries,” Comput. Meth. Appl. Mech. Eng. 2006; 195, pp. 3776–37961

Womersley J. R. “Method for the Calculation of Velocity, Rate of Flow and Viscous Drag in Arteries When the Pressure Gradient Is Known,” J. Physiol. 1955; 127(3), pp. 553–563

Zarins C. K., Zatina M. A., Giddens D. P., Ku D. N., and Glagov S. “Shear Stress Regulation of Artery Lumen Diameter in Experimental Atherogenesis,” J. Vasc. Surg. 1987; 5(3), pp. 413–420

Zikanov, O. (2010). Essential Computational Fluid Dynamics. Hoboken, NJ: John Wiley & Sons, Inc.

CHAPTER 7

APPENDIX A: Supplemental Tables and Figures

This chapter presents figures and tables of the raw data generated in this study

Table 7.1 below highlights the reported mesh quality metrics from ANSYS workbench. All four subjects had an average skewness value within the range considered to be “Excellent” and an orthogonal value within the range considered to be “Very good” by ANSYS.

Table 7.1 Final used mesh metrics along with color coded quality confirmations

Patient #	Elements	Skewness			Orthogonal Quality		
		Min	*Max*	*Average*	*Min*	*Max*	*Average*
14	591,597	0.00030009	0.8136	0.22626	0.25691	0.99621	0.86011
16	2,010,633	0.00013017	0.79848	0.2251	0.24318	0.99695	0.86082
17	1,311,684	0.00040195	0.79972	0.22458	0.24171	0.9964	0.86096
18	1,338,931	0.0005093	0.79941	0.22271	0.23179	0.99662	0.86209

Skewness mesh metrics spectrum

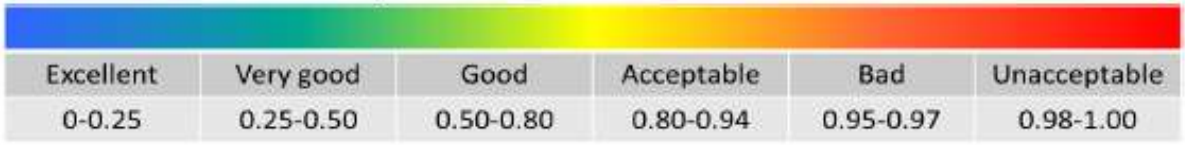

Excellent	Very good	Good	Acceptable	Bad	Unacceptable
0-0.25	0.25-0.50	0.50-0.80	0.80-0.94	0.95-0.97	0.98-1.00

Orthogonal Quality mesh metrics spectrum

Unacceptable	Bad	Acceptable	Good	Very good	Excellent
0-0.001	0.001-0.14	0.15-0.20	0.20-0.69	0.70-0.95	0.95-1.00

Figure 7.1 shows both the final model as well as the final generated mesh of subject 14. The subset of the bottom image, is simply a zoomed in section of the mesh.

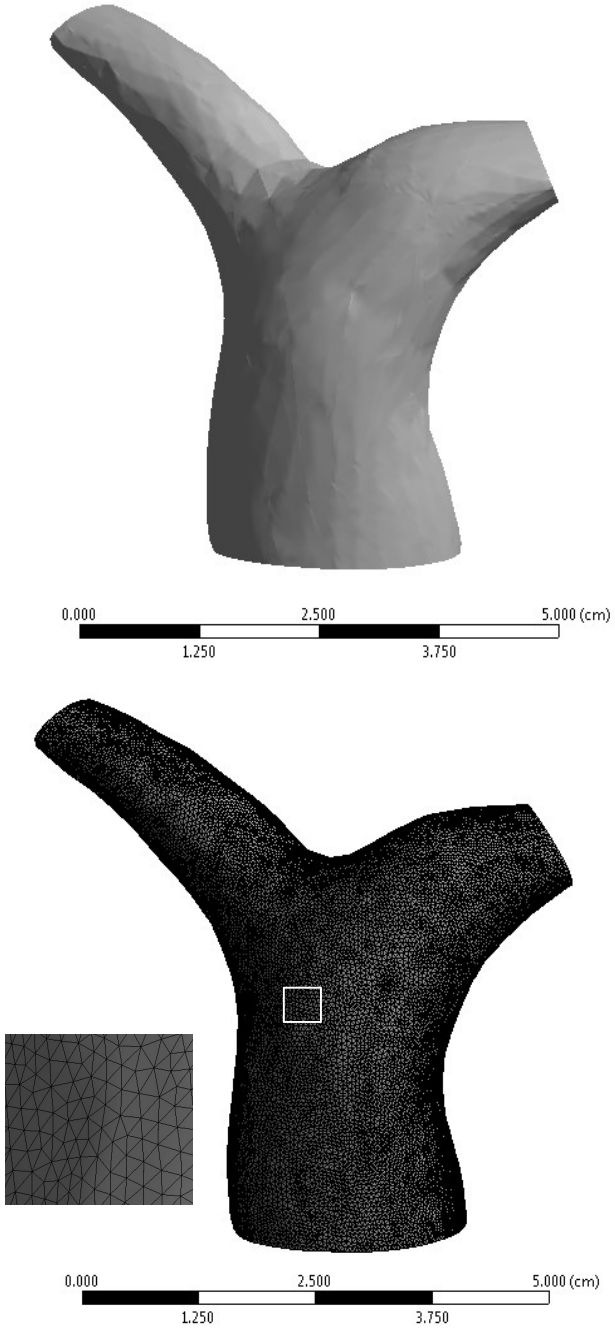

Figure 7.1: Final 3D geometry (top) along with the final mesh (bottom) of Patient 14.

Figure 7.2 shows both the final model as well as the final generated mesh of subject 16. The subset of the bottom image, is simply a zoomed in section of the mesh.

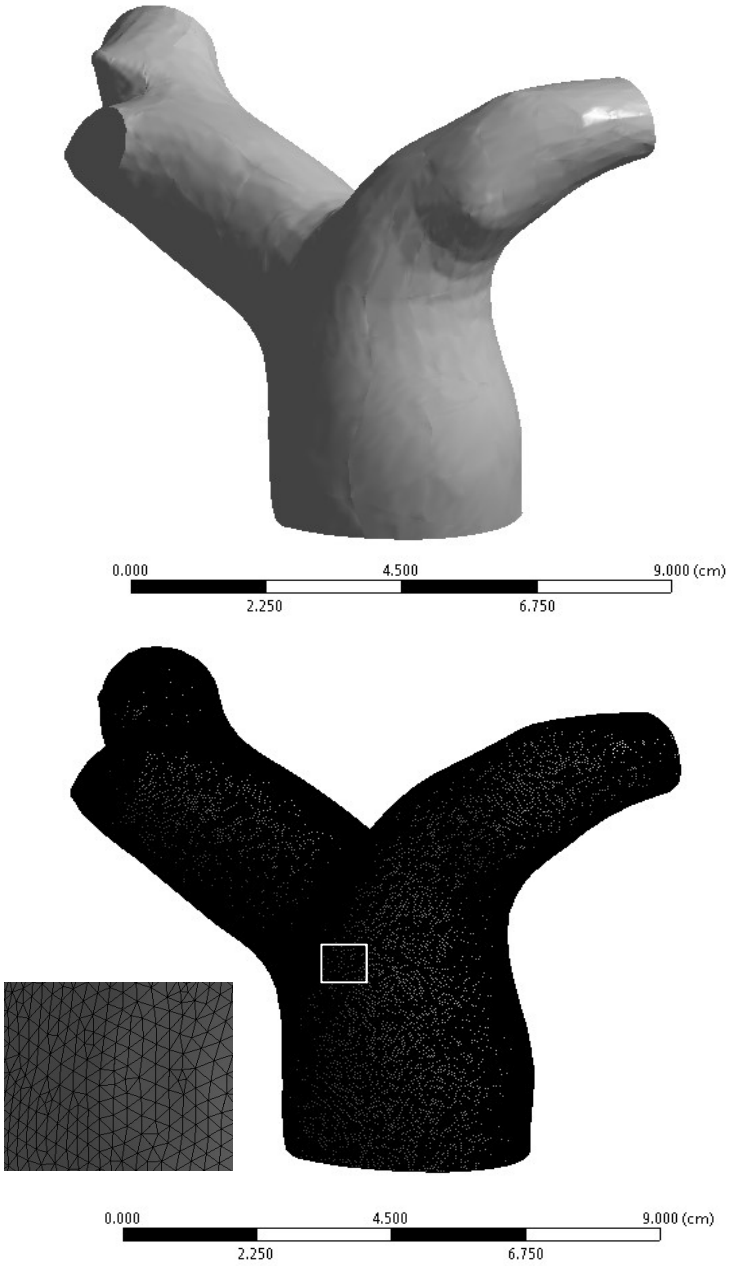

Figure 7.2: Final 3D geometry (top) along with the final mesh (bottom) of Patient 16.

Figure 7.3 shows both the final model as well as the final generated mesh of subject 17. The subset of the bottom image, is simply a zoomed in section of the mesh.

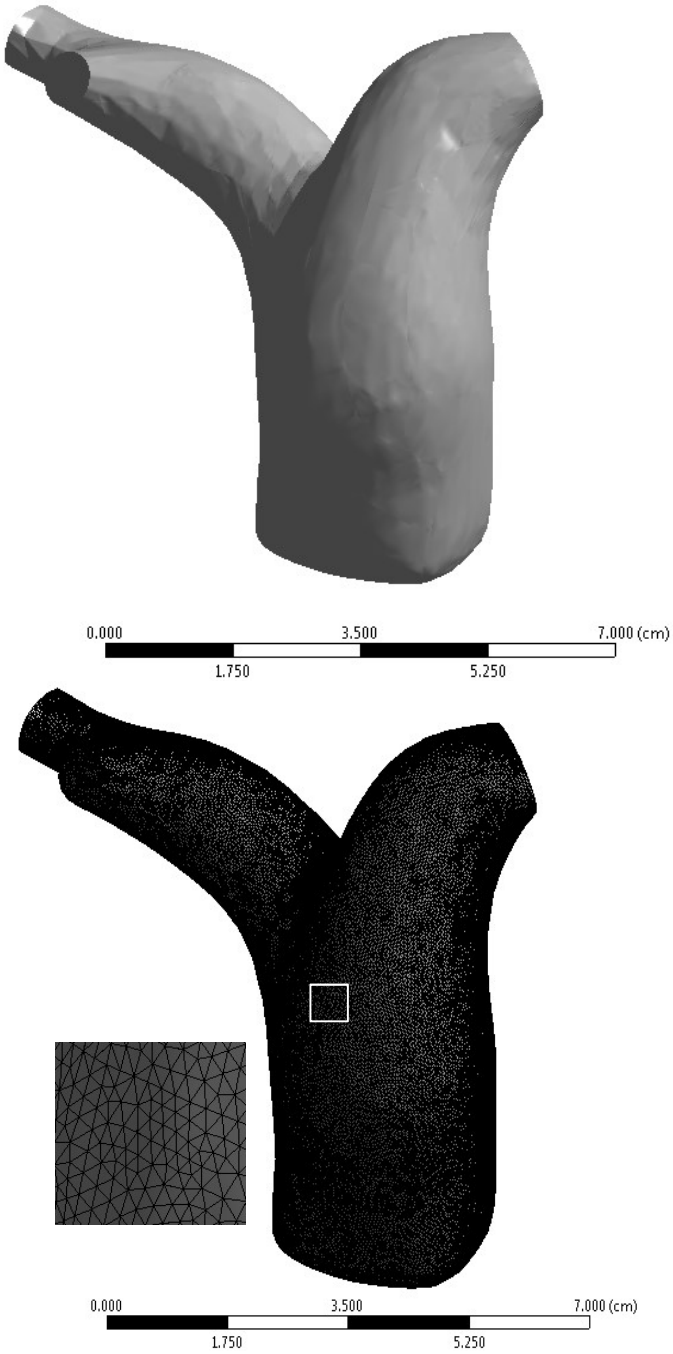

Figure 7.3: Final 3D geometry (top) along with the final mesh (bottom) of Patient 17.

Figure 7.4 shows both the final model as well as the final generated mesh of subject 18. The subset of the bottom image, is simply a zoomed in section of the mesh.

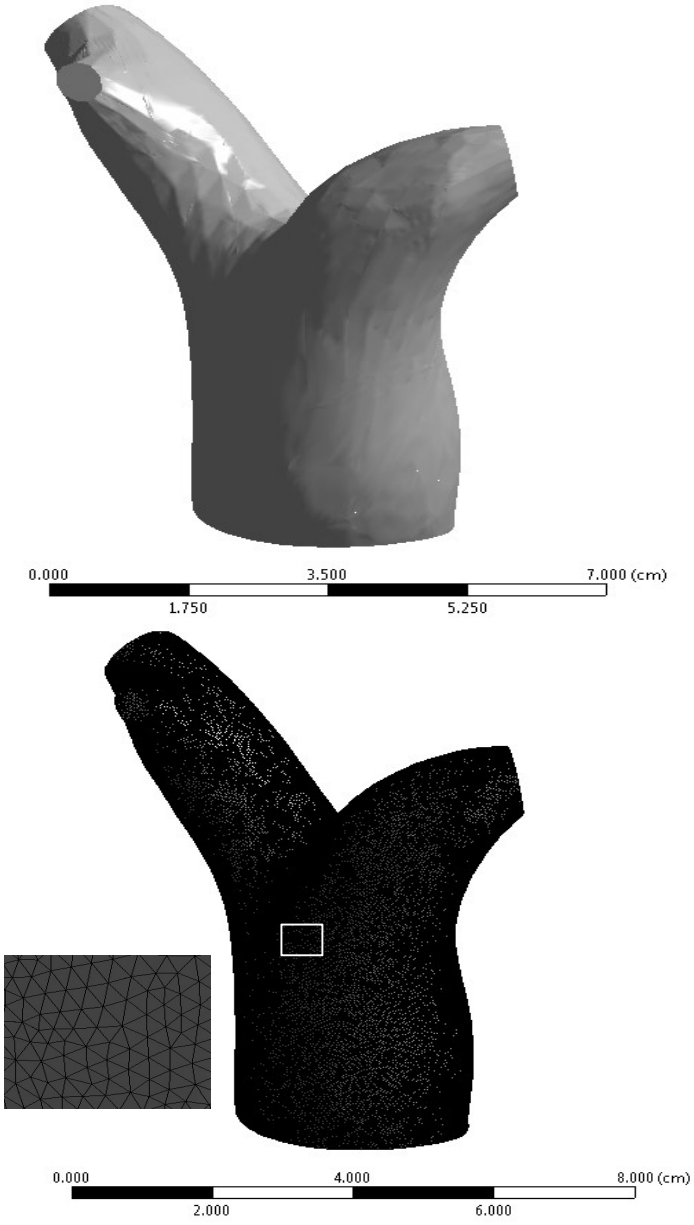

Figure 7.4: Final 3D geometry (top) along with the final mesh (bottom) of Patient 18.

Table 7.2 represents the inputs needed to achieve the various mesh sizes used in the mesh independence testing. Although different mesh densities were achieved, the sizes relative to the overall size of the geometries are the same.

Table 7.2 Mesh inputs used in mesh independence tests

Mesh Sizes	*Start*	*Fine*	*Finer*	*Finest*
Min Size	.1 cm	.05 cm	.05 cm	.035 cm
Max Face Size	.2 cm	.1 cm	.075 cm	.5 cm
Min Tetrahedral Size	.4 cm	.2 cm	.2 cm	.2 cm

Table 7.3 shows the final results of the mesh independence testing where percent differences were calculated between peak velocities for the varying mesh densities. Mesh independence was considered to be achieved when there was less than a one percent difference between mesh sizes.

Table 7.3 Mesh independence tests results

Patient 14		
Elements	Max Velocity @ Peak Systole (m/s)	% Difference
78,251		
275,020	1.886099	
313,656	1.889576	0.18417899
591,597	1.873823	0.83716874
Patient 16		
Elements		
256,067		
688,959	1.071019	
1,005,925	1.060415	0.99501087
2,010,633	1.062243	0.17223688
Patient 17		
Elements		
174,483		
515,724	0.8387666	
677,969	0.8287327	1.20346677
1,311,684	0.8255563	0.38401996
Patient 18		
Elements		
167,051		
483,020	0.8021042	
575,213	0.7981541	0.4936828
1,338,931	0.802554	0.5497442

Table 7.4 Summary of MRI Calculated Velocity Data for subject 14 where the yellow highlighted column represents the velocity inputs in cm/s for the Fluent simulations

Time	Area (cm^2)	Velocity (cm/s)	Flow Rate (ml/min)	Flow Rate (cm^3/s)	Diameter (cm)	Velocity (m/s)	Flow Rate/Area (m/s)
1	6.76	-1.43	-580.86	9.87	2.93	0.0143	0.0226
2	6.17	-20.18	-7466.51	126.93	2.80	0.2018	0.2910
3	5.73	-43.92	-15108.86	256.85	2.70	0.4392	0.5889
4	5.73	-55.88	-19221.43	326.76	2.70	0.5588	0.7492
5	6.32	-55.89	-21201.59	360.43	2.84	0.5589	0.8264
6	5.98	-54.63	-19606.38	333.31	2.76	0.5463	0.7642
7	6.29	-46.56	-17575.88	298.79	2.83	0.4656	0.6850
8	5.76	-39.39	-13623.30	231.60	2.71	0.3939	0.5310
9	6.14	-29.46	-10844.96	184.36	2.80	0.2946	0.4227
10	5.95	-22.82	-8148.32	138.52	2.75	0.2282	0.3176
11	5.24	-15.60	-4900.94	83.32	2.58	0.1560	0.1910
12	5.30	-0.16	-51.72	0.88	2.60	0.0016	0.0020
13	5.14	10.96	3383.60	-57.52	2.56	-0.1096	-0.1319
14	5.18	6.08	1889.38	-32.12	2.57	-0.0608	-0.0736
15	5.33	-1.22	-390.92	6.65	2.61	0.0122	0.0152
16	5.45	-5.07	-1660.50	28.23	2.64	0.0507	0.0647
17	5.27	-7.23	-2285.86	38.86	2.59	0.0723	0.0891
18	4.99	-7.75	-2319.44	39.43	2.52	0.0775	0.0904
19	5.02	-5.95	-1793.62	30.49	2.53	0.0595	0.0699
20	5.39	-3.17	-1025.67	17.44	2.62	0.0317	0.0400
21	5.05	-2.33	-706.17	12.00	2.54	0.0233	0.0275
22	5.05	-2.12	-641.55	10.91	2.54	0.0212	0.0250
23	5.30	-2.47	-785.10	13.35	2.60	0.0247	0.0306
24	5.39	-2.24	-724.06	12.31	2.62	0.0224	0.0282
25	5.95	-1.68	-598.88	10.18	2.75	0.0168	0.0233
26	6.45	-1.96	-757.08	12.87	2.86	0.0196	0.0295
27	6.07	-4.48	-1631.58	27.74	2.78	0.0448	0.0636
28	6.45	-3.81	-1474.44	25.07	2.86	0.0381	0.0575
29	6.17	-0.45	-167.84	2.85	2.80	0.0045	0.0065
30	6.01	2.45	882.26	-15.00	2.77	-0.0245	-0.0344
Avg.	5.70	-13.95	-4770.42	81.10	2.69	0.1395	0.1859
				Model Area	436.1617	mm^2	
					4.361617	cm^2	

Table 7.5 Summary of MRI Calculated Velocity Data for subject 16 where the yellow highlighted column represents the velocity inputs in cm/s for the Fluent simulations

Time	Area (cm^2)	Velocity (cm/s)	Flow Rate (ml/min)	Flow Rate (cm^3/s)	Diameter (cm)	Velocity (m/s)	Flow Rate/Area (m/s)
1	13.54	2.52	2046.09	-34.78	4.15	-0.0252	-0.0261
2	12.63	-7.53	-5709.11	97.05	4.01	0.0753	0.0730
3	12.54	-27.40	-20623.40	350.60	4.00	0.2740	0.2636
4	12.50	-43.13	-32348.04	549.92	3.99	0.4313	0.4134
5	12.63	-43.59	-33036.80	561.63	4.01	0.4359	0.4222
6	13.02	-36.06	-28171.00	478.91	4.07	0.3606	0.3600
7	12.89	-29.27	-22635.61	384.81	4.05	0.2927	0.2893
8	12.93	-26.32	-20429.19	347.30	4.06	0.2632	0.2611
9	12.93	-24.19	-18775.75	319.19	4.06	0.2419	0.2400
10	12.98	-21.45	-16703.45	283.96	4.06	0.2145	0.2135
11	13.15	-16.76	-13222.27	224.78	4.09	0.1676	0.1690
12	12.80	-9.61	-7385.33	125.55	4.04	0.0961	0.0944
13	12.67	1.12	849.95	-14.45	4.02	-0.0112	-0.0109
14	12.98	9.90	7705.76	-131.00	4.06	-0.0990	-0.0985
15	13.41	8.35	6721.69	-114.27	4.13	-0.0835	-0.0859
16	12.46	5.06	3783.65	-64.32	3.98	-0.0506	-0.0484
17	12.24	3.44	2524.80	-42.92	3.95	-0.0344	-0.0323
18	12.02	2.81	2024.46	-34.42	3.91	-0.0281	-0.0259
19	12.02	1.34	968.40	-16.46	3.91	-0.0134	-0.0124
20	11.68	0.38	267.51	-4.55	3.86	-0.0038	-0.0034
21	11.76	-0.06	-43.26	0.74	3.87	0.0006	0.0006
22	12.11	0.41	296.40	-5.04	3.93	-0.0041	-0.0038
23	12.20	0.81	594.63	-10.11	3.94	-0.0081	-0.0076
24	12.07	1.31	949.92	-16.15	3.92	-0.0131	-0.0121
25	12.63	1.09	827.41	-14.07	4.01	-0.0109	-0.0106
26	12.76	-0.68	-523.11	8.89	4.03	0.0068	0.0067
27	13.06	-1.51	-1180.23	20.06	4.08	0.0151	0.0151
28	13.50	0.04	35.31	-0.60	4.15	-0.0004	-0.0005
29	14.76	3.27	2895.76	-49.23	4.33	-0.0327	-0.0370
30	13.89	5.01	4173.32	-70.95	4.21	-0.0501	-0.0533
Avg.	12.76	-8.02	-6142.56	104.42	4.03	0.0802	0.0785
				Model Area	13.3019372	cm^2	
					1330.19372	mm^2	

Table 7.6 Summary of MRI Calculated Velocity Data for subject 17 where the yellow highlighted column represents the velocity inputs in cm/s for the Fluent simulations

Time	Area (cm^2)	Velocity (cm/s)	Flow Rate (ml/min)	Flow Rate (cm^3/s)	Diameter (cm)	Velocity (m/s)	Flow Rate/Area (m/s)
1	9.98	0.01	5.10	-0.09	3.57	-0.0001	-0.0001
2	9.60	-2.72	-1566.12	26.62	3.50	0.0272	0.0384
3	9.98	-9.52	-5703.38	96.96	3.57	0.0952	0.1398
4	10.20	-18.86	-11538.76	196.16	3.60	0.1886	0.2829
5	10.83	-19.77	-12845.23	218.37	3.71	0.1977	0.3149
6	11.14	-16.47	-11010.47	187.18	3.77	0.1647	0.2699
7	11.60	-12.36	-8602.57	146.24	3.84	0.1236	0.2109
8	11.29	-11.98	-8109.98	137.87	3.79	0.1198	0.1988
9	11.46	-9.66	-6642.68	112.93	3.82	0.0966	0.1628
10	11.60	-7.46	-5193.73	88.29	3.84	0.0746	0.1273
11	11.53	-2.48	-1717.59	29.20	3.83	0.0248	0.0421
12	10.93	1.42	930.49	-15.82	3.73	-0.0142	-0.0228
13	10.69	0.97	623.20	-10.59	3.69	-0.0097	-0.0153
14	10.93	0.29	187.39	-3.19	3.73	-0.0029	-0.0046
15	10.86	-0.79	-517.90	8.80	3.72	0.0079	0.0127
16	10.48	-1.17	-737.41	12.54	3.65	0.0117	0.0181
17	10.51	-0.84	-527.86	8.97	3.66	0.0084	0.0129
18	10.34	-0.64	-396.84	6.75	3.63	0.0064	0.0097
19	10.02	-0.34	-204.12	3.47	3.57	0.0034	0.0050
20	10.13	0.21	127.04	-2.16	3.59	-0.0021	-0.0031
21	9.67	-0.20	-114.30	1.94	3.51	0.0020	0.0028
22	9.56	-0.36	-204.03	3.47	3.49	0.0036	0.0050
23	9.74	-0.23	-135.06	2.30	3.52	0.0023	0.0033
24	9.60	-0.24	-135.66	2.31	3.50	0.0024	0.0033
25	9.70	-0.63	-368.38	6.26	3.51	0.0063	0.0090
26	9.70	-0.68	-394.06	6.70	3.51	0.0068	0.0097
27	9.53	-0.71	-408.52	6.94	3.48	0.0071	0.0100
28	9.42	-1.38	-777.45	13.22	3.46	0.0138	0.0191
29	9.00	-1.34	-725.31	12.33	3.39	0.0134	0.0178
30	8.72	0.11	59.42	-1.01	3.33	-0.0011	-0.0015
Avg.	10.29	-3.93	-2425.04	41.23	3.62	0.0393	0.0594
				Model Area	693.457	mm^2	
					6.93457	cm^2	

Table 7.7 Summary of MRI Calculated Velocity Data for subject 18 where the yellow highlighted column represents the velocity inputs in cm/s for the Fluent simulations

Time	Area (cm^2)	Velocity (cm/s)	FlowRate (ml/min)	Flow Rate (cm^3/s)	Diameter (cm)	Velocity (m/s)	Flow Rate/Area (m/s)
1	9.72	1.51	882.07	-15.00	3.52	0.0151	-0.0176
2	8.97	-0.39	-207.37	3.53	3.38	-0.0039	0.0041
3	9.06	-6.05	-3289.98	55.93	3.40	-0.0605	0.0655
4	10.07	-12.18	-7357.51	125.08	3.58	-0.1218	0.1464
5	10.60	-15.12	-9617.09	163.49	3.67	-0.1512	0.1914
6	10.51	-16.49	-10392.08	176.67	3.66	-0.1649	0.2068
7	10.60	-16.41	-10436.32	177.42	3.67	-0.1641	0.2077
8	10.44	-14.54	-9111.48	154.90	3.65	-0.1454	0.1813
9	10.88	-11.12	-7260.11	123.42	3.72	-0.1112	0.1445
10	11.48	-8.36	-5756.84	97.87	3.82	-0.0836	0.1146
11	10.69	-7.22	-4631.19	78.73	3.69	-0.0722	0.0922
12	10.72	-5.13	-3303.95	56.17	3.70	-0.0513	0.0658
13	10.32	-2.34	-1446.30	24.59	3.62	-0.0234	0.0288
14	10.82	0.79	511.23	-8.69	3.71	0.0079	-0.0102
15	10.25	4.00	2463.47	-41.88	3.61	0.0400	-0.0490
16	10.51	4.58	2885.33	-49.05	3.66	0.0458	-0.0574
17	10.44	2.00	1252.70	-21.30	3.65	0.0200	-0.0249
18	10.16	-0.17	-102.07	1.74	3.60	-0.0017	0.0020
19	10.25	-0.71	-434.34	7.38	3.61	-0.0071	0.0086
20	10.00	-1.08	-646.34	10.99	3.57	-0.0108	0.0129
21	10.00	-0.28	-166.98	2.84	3.57	-0.0028	0.0033
22	9.66	0.16	91.53	-1.56	3.51	0.0016	-0.0018
23	9.63	-0.63	-364.06	6.19	3.50	-0.0063	0.0072
24	9.75	-0.76	-442.77	7.53	3.52	-0.0076	0.0088
25	9.88	-0.37	-216.84	3.69	3.55	-0.0037	0.0043
26	9.38	-0.56	-315.27	5.36	3.46	-0.0056	0.0063
27	9.60	0.08	48.16	-0.82	3.50	0.0008	-0.0010
28	9.22	0.56	310.52	-5.28	3.43	0.0056	-0.0062
29	9.31	0.75	419.91	-7.14	3.44	0.0075	-0.0084
30	8.97	0.81	436.82	-7.43	3.38	0.0081	-0.0087
Avg.	10.06	-3.49	-2106.06	35.80	3.58	-0.0349	0.0419
				Model Area	8.5420025	cm^2	
					854.20025	mm^2	

Table 7.8 Summary of Mesh Data Post Increasing Mesh Density Near the Wall

Patient #	Elements	Skewness			Orthogonal Quality		
		Min	*Max*	*Average*	*Min*	*Max*	*Average*
14	717,000	0.000174004	0.82716	0.21252	0.23464	0.99971	0.88989
16	2,352,700	0.00022508	0.96227	0.21015	0.03772	0.99985	0.88818
17	1,550,000	0.00032596	0.79821	0.21073	0.22835	0.9994	0.88856
18	1,560,000	0.000414173	0.80787	0.20931	0.23511	0.99978	0.88823

APPENDIX B: IRB Approval

EAST CAROLINA UNIVERSITY
University & Medical Center Institutional Review Board Office
4N-70 Brody Medical Sciences Building· Mail Stop 682
600 Moye Boulevard · Greenville, NC 27834
Office 252-744-2914 · Fax 252-744-2284 · www.ecu.edu/ORIC/irb

Notification of Continuing Review Approval: Expedited

From: Biomedical IRB
To: John Cahill
CC: Sanjay mehra
Date: 6/1/2017
Re: CR00006031
UMCIRB 11-0275
[IMPORTED] Investigation of Pulmonary Artery Hypertension Using MRI and Computational Fluid Dynamics

The continuing review of your expedited study was approved. Approval of the study and any consent form(s) is for the period of 6/1/2017 to 5/31/2018. This research study is eligible for review under expedited categories #4 and#5. The Chairperson (or designee) deemed this study no more than minimal risk.

Changes to this approved research may not be initiated without UMCIRB review except when necessary to eliminate an apparent immediate hazard to the participant. All unanticipated problems involving risks to participants and others must be promptly reported to the UMCIRB. The investigator must submit a continuing review/closure application to the UMCIRB prior to the date of study expiration. The Investigator must adhere to all reporting requirements for this study.

Approved consent documents with the IRB approval date stamped on the document should be used to consent participants (consent documents with the IRB approval date stamp are found under the Documents tab in the study workspace).

The approval includes the following items:

Document	Description
Revised Consent Form(0.03)	Consent Forms

The Chairperson (or designee) does not have a potential for conflict of interest on this study.